We detected 48 ROIs out of the 170 ROIs, which indicated sufficient numbers of spiking events (0.03–1 Hz, Fig. 1E). We confirmed these 48 ROIs corresponded to neuronal soma by visually inspecting them. The peaks of the neuronal Ca2+ spikes were found to have similar intensities, and we observed no buildup activities (Fig. 1D). We therefore deemed it safe to interpret each Ca2+ spike with a width of 10 ms to be a single spike. As such, the activity over each of the 48 ROIs was recorded as a binary time series.

We selected six ROIs, other than the 48 neuronal ROIs, as regions representing glial cells, based on their morphologies (by visual inspection) and fluorescence levels. We particularly selected small cells with high fluorescence levels because such cells were likely to be astrocytes [34]. The radius of each ROI was re-set individually to a smaller value than that of the neurons because we only found six glial ROIs. We used the signal average over each glial ROI as the measure of glial activity (Fig. 1G) and arranging it over 60,000 frames constituted the activity time series. We applied individual linear detrending to each glial time series to remove slow trends possibly induced by photo-bleaching. We then applied a temporal Gaussian filter ($\sigma = 500$ms) to remove high frequency noise and shot noise. The glial time series thus obtained is depicted in Fig. 1H. We assumed that the activity of astrocytes had a linear relationship in the analysis that followed with the signal intensity measured by Ca2+ imaging.

Generative model and MAP estimation

Generative modeling was adopted to statistically describe the Ca2+ signals of neurons and glial cells. We introduced a prior distribution to avoid overfitting due to the finite/small size of collected data in the experiments. The model parameters were estimated with the MAP method.

Let t index the image sampling time over the observation, $t = 1, \ldots, T$; in our particular case, $T = 60,000$. We have activity series of neurons $\{N_i(t) | i = 1, \ldots, n\}$ and glial cells $\{G_j(t) | j = 1, \ldots, m\}$ after preprocessing, where $n(=48)$ and $m(=6)$ correspond to the numbers of neuronal and glial ROIs. As glial activity is continuous, $G_j(t)$ is a series of discrete values sampled from a continuous function of time. $N_i(t)$ can be seen as a unit point process; $N_i(t) = 1$ when the i-th neuron emits a spike at time t, or $N_i(t) = 0$ otherwise. Our sampling interval was 10 ms within which every neuron was well assumed to have produced at most one spike in our imaging experiment (see 'Pre-processing' section). We normalized the activity time series of the j-th glial cell $G_i(t)$ individually, so that its average was zero and variance was one. This normalization was performed because glial cells exhibited different initial fluorescence levels due to variations in light absorption. For simplicity, let $Y(t)$ denote the activities of all the elements, $Y(t) \equiv (N_1(t), \ldots, N_n(t), G_1(t), \ldots, G_m(t))^T$, where T is a transpose. The vector, $\mathbf{Y} \equiv (Y(1), \ldots, Y(T))^T$, will be called the observation time series after this. We assumed that $\mathbf{Y}$ would obey a stationary and conditionally independent Markov chain of order h, which included an autoregressive process of order h as a special case. When we use the term Markov, our models of interest may include those in which the dependence of the current state on past states is non-linear.

Below, we provide the likelihood of $\mathbf{Y}$, $p(\mathbf{Y}|\theta)$ based on our generative model, where θ is the parameter vector. Let $p(\theta)$ be its prior distribution. Bayes' theorem tells us that the posterior distribution of the parameter vector is given by $p(\theta|\mathbf{Y}) \propto p(\mathbf{Y}|\theta)p(\theta)$. Given an observation time series, $\mathbf{Y}$, the parameter-vector estimate, $\hat{\theta}(\mathbf{Y})$, is the θ that maximizes the posterior distribution (i.e., the MAP estimation). Our generative model is

based on a Markov chain model where the neuronal and glial activities at present are assumed to be mutually independent but dependent on their past activities. More precisely, $p(\mathbf{Y}|\theta) = \Pi_{t=1}^{T}$ $\left(\Pi_{i=1}^{n} p(N_i(t)|\mathcal{H}_t^Y, \theta_i^N) \right) \left(\Pi_{j=1}^{m} p(G_j(t)|\mathcal{H}_t^Y, \theta_j^G) \right)$, where $\mathcal{H}_t^Y \equiv (Y(t-1), \ldots, Y(t-h))$ is the history of activities of all the components with a maximum time lag, $h > 0$. We allowed all neurons to have their own parameters θ_i^N and all glial cells to have their own parameters θ_j^G. That is, $\theta \equiv (\theta_1^N, \ldots, \theta_n^N, \theta_1^G, \ldots, \theta_m^G)$. Moreover, the maximum time lag, h, could be differently set for individual types of interactions (see below).

A spike production by the i-th neuron with a fixed time interval was assumed to obey a Bernoulli process with logistic regression [32,70]

$$p(N_i(t)|\mathcal{H}_t^Y, \theta_i^N) = \pi_i(t)^{N_i(t)}(1 - \pi_i(t))^{1 - N_i(t)}, \qquad (1a)$$

$$\log \frac{\pi_i(t)}{1 - \pi_i(t)} = r_i + \sum_{j=1}^{n} \sum_{s=1}^{h_a} a_{ij}(s) N_j(t-s) + \\ \sum_{j=1}^{m} \sum_{s=1}^{h_b} b_{ij}(s) G_j(t-s), \qquad (1b)$$

where h_a denotes the maximum time lag (history window sizes) from neurons and h_b denotes the maximum time lag from glial cells (Fig. 2A). The generative model above is an instance of GLMs, in which the parameter vector of neuron i is given by $\theta_i^N \equiv \{\mathbf{a}_i \equiv (a_{ij}(s)), \mathbf{b}_i \equiv (b_{ij}(s')), r_i | j = 1, \ldots, n, s = 1, \ldots, h_a, s' = 1, \ldots, h_b\}$, where r_i represents the spontaneous firing rate of neuron i, and $a_{ij}(s)$ and $b_{ij}(s)$ denote the response functions from neuron j to neuron i and from glial cell j to neuron i, which are defined over the history window sizes h_a and h_b, respectively.

The activity of glial cell i is given by a vector autoregressive (VAR) model disturbed by white Gaussian observation noise, which is another instance of GLMs. More precisely,

$$p(G_i(t)|\mathcal{H}_t^Y, \theta_i^G) = \frac{1}{\sqrt{2\pi\sigma_i^2}} \exp\left\{ \frac{(G_i(t) - \mu_i(t))^2}{2\sigma_i^2} \right\}, \qquad (2a)$$

$$\mu_i(t) = v_i + \sum_{j=1}^{n} \sum_{s=1}^{h_c} c_{ij}(s) N_j(t-s) + \sum_{j=1}^{m} \sum_{s=1}^{h_d} d_{ij}(s) G_j(t-s), \qquad (2b)$$

where h_c denotes the maximum time lags (history window sizes) from neurons and h_d denotes the maximum time lags from glial cells. The parameter vector of glial cell i in this VAR model is given by $\theta_i^G \equiv \{\mathbf{c}_i = (c_{ij}(s)), \mathbf{d}_i = (d_{ij}(s')), v_i, \sigma_i | j = 1, \ldots, n, s = 1, \ldots, h_c, s' = 1, \ldots, h_d\}$, where v_i is the bias of glial cell i and σ_i is its variance. Also, $c_{ij}(s)$ and $d_{ij}(s)$ denote the response functions from neuron j to glial cell i and from glial cell j to glial cell i, which are defined over the history window sizes h_c and h_d, respectively. We have used the notations, $\mathbf{a} \equiv \{\mathbf{a}_i\}_{i=1}^{n}$, $\mathbf{b} \equiv \{\mathbf{b}_i\}_{i=1}^{n}$, $\mathbf{c} \equiv \{\mathbf{c}_j\}_{j=1}^{m}$ and $\mathbf{d} = \{\mathbf{d}_j\}_{j=1}^{m}$, in this paper to represent the sets of response functions between neurons, from glial cells to neurons, from neurons to glial cells, and between glial cells, respectively. The whole GLM for the neuron-glia system above is a state-space model with internal deterministic processes based on a combination of logistic regression and VAR models. The model reduces to

a couple of independent GLMs if there are no interactions between the neuronal and glia networks, i.e., $\mathbf{b} = \mathbf{c} = \mathbf{0}$.

Prior distribution

Here, we explain our prior setting of the model parameters in our GLM. We introduced a prior distribution to the parameters representing the response functions, $\mathbf{a}, \mathbf{b}, \mathbf{c}$ and $\mathbf{d}$, to make the response functions sparse, which is preferred in avoiding over-fitting to relatively small datasets, in addition to smoothing with respect to the lag time. Such a prior distribution is given by

$$p^{\mathrm{sm}}(f_{ij}(\cdot)) \propto \exp\left\{ -\sum_{s=1}^{h_f} \lambda_f |f_{ij}(s)|^2 + \lambda_f^{\mathrm{sm}} |f_{ij}(s) - f_{ij}(s-1)|^2 \right\}, \quad (3)$$

$f = a, b, c$ or d,

where tuning constant λ_f controls the L2-sparseness of the response functions and λ_f^{sm} controls their smoothness. We granted independent, noninformative priors $p(r_i) = p(v_i) = \mathrm{const.}$ and $p(\sigma_i) = 1/\sigma_i$ to parameters r_i, v_i and σ_i (Eqs. (1) and (2)). In summary, we put $p(\theta) = \Pi_{i=1}^n p(\theta_i^N) \Pi_{j=1}^m p(\theta_j^G)$, $p(\theta_i^N) = p(r_i) \Pi_{j=1}^n p(a_{ij}) \Pi_{j=1}^m p(b_{ij})$, and $p(\theta_i^G) = p(v_i) p(\sigma_i) \Pi_{j=1}^n p(c_{ij}) \Pi_{j=1}^m p(d_{ij})$. These parameters and their prior distribution are summarized in Table S3.

The prior based on L2-sparseness would be preferable for increasing the cross-validated likelihood of the model [71] by effectively reducing the sensitivity of the model to noise inevitably involved in a relatively small dataset. The smoothness prior would reduce the effective space in which the response functions exist and hence would be beneficial to improve the cross-validated likelihood. Although the time scales of neuron-glia interactions may span a wide range, fluctuating from several tens of milliseconds to several hours [6,12,14], our current study focused on specific types of interactions that lasted for several hundreds of milliseconds. Our prior setting that preferred smooth response functions was also considered to work in removing neuron-glia interactions with shorter time scales.

Efficient estimation of parameters

By applying Bayes' theorem to the likelihood and the prior distribution above, we have the following log posterior

$$\log p(\theta|Y) \propto \sum_{i=1}^n \log\left\{ \prod_{t=1}^T p(N_i(t)|\mathcal{H}_t^Y, \theta_i^N) p(\theta_i^N) \right\} + \sum_{j=1}^m \log\left\{ \prod_{t=1}^T p(G_j(t)|\mathcal{H}_t^Y, \theta_j^G) p(\theta_j^G) \right\}. \quad (4)$$

We obtained the parameter vector, θ, that maximized the log posterior above; the expression above suggests that this MAP estimation can be individually performed for each $\theta_i^N (i = 1, \ldots, n)$ and for each $\theta_j^G (j = 1, \ldots, m)$. This individuality also suggests the ability to apply parallel computation to the estimation of parameters.

Fortunately, our set of MAP estimates is unique because our generative model is an instance of GLM [72] and a strictly convex prior distribution also makes the posterior distribution convex. This allows us to use efficient optimization algorithms. When maximizing the first term in Eq. (4) with respect to θ_i^N, we used a

limited-memory Broyden-Fletcher-Goldfarb-Shanno (BFGS) method [73], which is a variation of a quasi-Newton method, to conserve the memory necessary for optimization. The second term in Eq. (4) is a convex quadratic function. We can therefore use a simple linear algebra to estimate θ_j^G.

Functional connectivity analysis

Our functional connectivity analysis between neurons and glial cells was based on a comparison of the cross-validated likelihood, i.e., the model's reproducibility for the activities in a validation dataset, between two different network structures. If there were two different network structures, one with a certain neuron-glia connection and another without the connection, and the latter demonstrated a larger cross-validated likelihood than the former, then, the connection was not considered to be included in our neuron-glia system. According to the K-fold cross-validation with K being 10, we partitioned the time series $\mathbf{Y}$ into 10 subseries; we used nine of these subseries to train the model ("training dataset"), and calculated the model-likelihood of the one remaining subseries ("test dataset") as the cross-validated likelihood of the model. The neuron-wise, test-dataset-wise cross-validated likelihood of the activity of the i-th neuron, evaluated on the k-th test dataset for a network structure, q, was given by $l_{i,k}^N(\mathbf{Y}, q) = \log \Pi_t p(N_i(t)| \mathcal{H}_t^Y, \hat{\theta}_i^N, q)$, where t indexes the re-arranged sampling time (sample number) in the k-th test dataset, and the parameter vector $\hat{\theta}_i^N$ was determined by using the training dataset other than the k-th test dataset under network structure q. By taking the average of the neuron-wise, test-dataset-wise cross-validated likelihood over the 10 test datasets, we have the neuron-wise cross-validated likelihood of the i-th neuron, $l_i^N(\mathbf{Y}, q)$. Then, taking the average over all the neurons, we have the cross-validated likelihood of network structure q as $l^N(\mathbf{Y}, q)$.

Similarly, we defined $l_{i,k}^G(\mathbf{Y}, q)$ as the glia-wise, test-dataset-wise cross-validated likelihood of the activity of the i-th glial cell evaluated on the k-th test dataset for network structure q. We also defined the i-th glia-wise cross-validated likelihood, $l_i^G(\mathbf{Y}, q)$, and likewise the cross-validated likelihood of network structure q as $l^G(\mathbf{Y}, q)$.

When evaluating the connections from the j-th glial cell to neurons, we compared the cross-validated likelihood between two different network structures, q_N and $q_{N \leftarrow G_j}$, to which different constraints were introduced. The constraint given to q_N was $\mathbf{b} = 0$, i.e., there were no connections from any glial cell to any neuron. The constraint given to $q_{N \leftarrow G_j}$ was $b_{ik}(s) = 0, k \neq j$ for all $i = 1, \ldots, n$, i.e., there were no connections from glial cells to neurons other than from the j-th glial cell. We evaluated the neuron-wise cross-validated likelihood, $l_i^N(\mathbf{Y}, q)$, $q \in \{q_N, q_{N \leftarrow G_j}\}$, for each of the two network structures after we had estimated their individual model parameters. Observe that $b_{ij}(s) = 0, s = 1, \ldots, T$ yields $\mathrm{E}[l_i^N(\mathbf{Y}, q_{N \leftarrow G_j}) - l_i^N(\mathbf{Y}, q_N)] = 0$, where the expectation is with respect to the GLM (Eq. (1)) with the true parameter vector plugged in. This observation suggests that we can use the difference in the cross-validated likelihood, $d_{ij}^{N \leftarrow G}(\mathbf{Y}) = \frac{1}{10} \sum_{k=1}^{10} \{l_{i,k}^N(\mathbf{Y}, q_{N \leftarrow G_j}) - l_{i,k}^N(\mathbf{Y}, q_N)\}$, to evaluate the effect from a specific functional connectivity from glial cell j to neuron i, which is represented by the response function, $b_{ij}(s)$.

As it is difficult to obtain the analytical form of the distribution for the stochastic variable, $d_{ij}^{N \leftarrow G}(\mathbf{Y})$, there is no theoretical way to perform a statistical test based on it. To construct a statistical test in a practical manner, therefore, we assumed that the difference in

the neuron-wise, test-dataset-wise cross-validated likelihood, $[l_{i,k}^N(\mathbf{Y},p_{N\leftarrow G_j}) - l_{i,k}^N(\mathbf{Y},p_N)]$, would obey a normal distribution with a zero mean and variance $\sigma_{d_{ij}^{N\leftarrow G}}$, and designed a t-statistic:

$$t_{ij}^{N\leftarrow G} \equiv \sqrt{10}d_{ij}^{N\leftarrow G}/\sigma_{d_{ij}^{N\leftarrow G}}, \qquad (5)$$

where $(\sigma_{d_{ij}^{N\leftarrow G}})^2$ is the unbiased variance of the difference in the cross-validated likelihood, $d_{ij}^{N\leftarrow G}$, calculated in the cross-validation process. By simply assuming the normality of the stochastic variable, $d_{ij}^{N\leftarrow G}(\mathbf{Y})$, we can make $t_{ij}^{N\leftarrow G}$ to follow a t-distribution. We can then rely on the standard t-test, when evaluating each connection from glial cell j to neuron i. Indeed, this t-statistic assumption is not very accurate because the cross-validation samples are not independent of one another and the stochastic variable does not obey a normal distribution. However, the advantages of the t-statistic assumption on $t_{ij}^{N\leftarrow G}$ outweigh the disadvantages; we can evaluate the stochastic uncertainty of $d_{ij}^{N\leftarrow G}(\mathbf{Y})$ up to the second order moment by using this token.

We took the opposite approach when evaluating connections from neurons to a particular single glial cell, i. We compared two different network structures in a similar way to that above with a fixed glial cell of interest, i.e., the i-th glial cell: the network with no neuronal connections to the glial cell (i.e., $c_{ij}(s) = 0, j = 1, \ldots, n$), and the network consisting of all possible connections. We defined the mean of differences in the glia-wise, test-dataset-wise cross-validated likelihood of the i-th glial cell by $d_{ij}^{G\leftarrow N}(\mathbf{Y}) = \frac{1}{10}\sum_{k=1}^{10}\{l_{i,k}^G(\mathbf{Y},q_{G\leftarrow N}) - l_{i,k}^G(\mathbf{Y},q_{G\leftarrow N_{-j}})\}$.

A t-statistic of the difference in the glia-wise cross-validated likelihood was similarly defined as

$$t_{ij}^{G\leftarrow N} = \sqrt{10}d_{ij}^{G\leftarrow N}/\sigma_{d_{ij}^{G\leftarrow N}}. \qquad (6)$$

We treated the connections from glia to neurons differently from those from neurons to glia in this study. The main principle of our search for the optimal network structure was to begin the search from a network structure with the highest cross-validated likelihood possible (see 'Methods Overview' section in Results. Some details are also given in Text S1). While the network structure with no neuron-to-glia connections exhibited a higher glia-wise cross-validated likelihood than the network structure with full neuron-to-glia connections (full network), the neuron-wise cross-validated likelihood of the full network was lower than that of the structure with no glia-to-neuron connections (Fig. S1). Also, we resorted to an incremental search algorithm by considering the intractability of a full search over the whole space of all possible network structures. The search algorithm we adopted converges to an optimal network structure if we begin the search from a heuristically chosen structure with a high cross-validated likelihood. The cross-validated likelihood of the network structure monotonically increases and necessarily converges in this search algorithm because we only adopt a new structure when the cross-validated likelihood increases whereas the number of possible network structures is huge but still finite.

Surrogate method

We explored a statistical test based on the surrogate method to statistically examine the number of detected connections under the null hypothesis of no causal connectivity. We need to construct surrogate neuronal or glial activities that might have been observed under the null hypothesis, only from the observation time series.

In order to evaluate the number of detected connections from the i-th glial cell to neurons, we generated the surrogate glial activity (Ca2+ signals) of the i-th glial cell (called the original glial cell below) 1000 times based on the Iterated Amplitude Adjusted Fourier Transform (IAAFT) method (for details, see Text S1) [74]. This surrogate glial cell was assumed to have no connections to any neurons in the neuron-glia system, but all other parts of the system remained untouched. Surrogate glial activity in the IAAFT method was generated based on the randomization of phases in the activity time series of the original glial cell. Application of IAAFT to glial activity destroyed the mutual correlation between the original glial cell and all the other network components while preserving the amplitude distribution and the autocorrelation of the activity of the original glial cell (see Fig. S2). We obtained 1000 surrogate datasets by replacing the activity time series of the original glial cell with each of the 1000 surrogate glial activities. We then applied functional connectivity analysis to each of the 1000 surrogate datasets and computed the number of detected connections from the surrogate glial cell to neurons. The empirical distribution constructed from the 1000 surrogate datasets could serve as a null distribution built on the hypothesis that there were no functional connectivities from the original glial cell to neurons. We compared the number of actually detected connections based on the original glial cell's activity against the empirical distribution to compute the p-value of the original glial cell's activity.

In the construction of each surrogate neuronal activity, on the other hand, we applied a circular shift to the original neuronal spike time series. This type of implementation is preferable [75] because it can perturb the temporal relationship between neurons, whose activities are surrogated, and other components of the network while preserving its own statistics, such as the distribution of inter-spike intervals, autocorrelation, and self-dependence of the original neuronal activity.

Tuning parameters

We determined the tuning parameters (tuning constants), $\{(h_f,\lambda_f,\lambda_f^{sm}); f = a,b,c,d\}$ to optimize the cross-validated likelihood by applying heuristic constraints to reduce the space to search for their optimal combination. The parameters to be tuned were maximum time lags (history window sizes) (h_a,h_b,h_c,h_d) under the heuristic constraints, $h_a = h_b$ and $h_c = h_d$, shrinkage parameters of the response functions $(\lambda_a,\lambda_b,\lambda_c,\lambda_d)$ under the heuristic constraints, $\lambda_a = \lambda_b$ and $\lambda_c = \lambda_d$, and smoothness parameters of the response functions $(\lambda_a^{sm},\lambda_b^{sm},\lambda_c^{sm},\lambda_d^{sm})$ under the heuristic constraints, $\lambda_a^{sm} = \lambda_b^{sm}$ and $\lambda_c^{sm} = \lambda_d^{sm}$. More concretely, we searched discretized candidates $\{5,10,20,40,$ and $80\}$ for the best values for both $h_a = h_b$ and $h_c = h_d$, $\{0,1,1,10,$ and $100\}$ for both $\lambda_a = \lambda_b$ and $\lambda_c = \lambda_d$, and $\{0.1,1,10,$ and $100\}$ for both $\lambda_a^{sm} = \lambda_b^{sm}$ and $\lambda_c^{sm} = \lambda_d^{sm}$, to maximize the cross-validated likelihoods, $l^N(\mathbf{Y},q_{N\leftarrow G})$ and $l^G(\mathbf{Y},q_{G\leftarrow N})$. Consequently, we found the optimal values for the tuning parameters were $(\lambda_a = \lambda_b,\lambda_c = \lambda_d) = (0.1,0.1)$, $(\lambda_a^{sm} = \lambda_b^{sm},\lambda_c^{sm}, = \lambda_d^{sm}) = (1,0.1)$, and $(h_a = h_b,h_c = h_d) = (40,5)$.

Here, we applied the heuristic constraints to mainly reduce the search space of the tuning parameters. Such application of constraints is equivalent to having assumed that similar mechanisms govern all receptors on neuronal and glial cells. However, some studies have indicated the possibility that glial receptors might respond differently to neurons and glia [15]. Therefore, we recomputed λ_c and λ_d independently (with no constraints) to

validate our heuristic constraint $\lambda_c = \lambda_d$, while clumping all the other tuning parameters, and we found that the recomputed parameter values were equal to that with the constraint $\lambda_c = \lambda_d$. When we carried out the same validation for the constraint, $h_c = h_d$, the optimal values without the constraint also yielded the same value as that with the constraint. Further, the overall characteristics of the response functions were found to be fairly robust against the large diversion in the smoothing parameter from its optimal value (Fig. S7).

Positivity constraints to response functions from neurons to glia

We attempted to introduce a specific constraint, $c_{ij}(s) > 0$ for any s, to our GLM, i.e., the connection from neuron i to glial cell j is required to be strictly positive. The parameter optimization (the MAP estimation) of the log posterior with our likelihood and prior distribution is equivalent to the minimization of a specific quadratic cost function. The parameter estimation under the additional constraint, $c_{ij}(s) > 0$ for any s, can then be performed by quadratic programming [76], so as to minimize the cost function under the constraint. Based on the $\hat{\theta}$ thus computed, we can compute the neuron-wise cross-validated likelihood, $l_i^N(Y,q)$ as well as t-statistic $t_{ij}^N(Y,q)$ for any network structure q. We explained how the introduction of the positivity constraint above affected the results of functional connectivity analysis at the end of the Discussion section.

Supporting Information

Figure S1 Model comparison based on cross-validated likelihood. We compared the models with different assumptions on the network structure, q (summarized in Tables S1 and S2), in terms of the cross-validated likelihood of the glial activities, $l^G(Y,q)$ (left panel), and that of the neuronal spikes, $l^N(Y,q)$ (right panel). Asterisks indicate the presence of statistically significant differences ($p < 0.05$, paired Student t-test).
(EPS)

Figure S2 Iterative amplitude adjusted Fourier transform (IAAFT) method. (A) The activity of a single glial cell (glia 2, left panel) and the activity surrogated from the original activity of the same cell by the IAAFT method (right panel). (B) Amplitude distribution and autocorrelation of the original and surrogate glial activities. Note that the amplitude distribution is the same between the original and the surrogate ones (left panels). The autocorrelations are also similar (right panels). (C) The cross correlation between a neuronal activity and a glial activity was destroyed by the IAAFT method. The left (middle) panel shows the phase diagram of the cross correlation between neuron 6 and glial cell 2 (surrogate glial cell 2), in which the abscissa and ordinate denote the activity of glial cell 2 and the spike frequency of neuron 6, respectively. We used bins of 5 s to calculate the spike frequency from the neuronal activity time series. The rightmost panel shows a histogram of the cross correlation coefficient, r, between all pairs of neurons and the surrogate glial cells (the latter are independent of other network components). Note that the histogram spans the range of $[-1,1]$ and has a mean of approximately 0. This indicates that the correlation is sufficiently randomized.
(EPS)

Figure S3 Detection of glia-to-neuron connections. Recall that $d_{ij}^{N \leftarrow G}$ is the gain in the cross-validated likelihood achieved by the addition of the connection from the j-th glial cell

to the i-th neuron, and $t_{ij}^{N \leftarrow G}$ is the t-statistics derived from $d_{ij}^{N \leftarrow G}$. The six panels depict $t_{ij}^{N \leftarrow G}$ for all pairs of i and j. Each panel corresponds to a single glial cell (different index of j) out of the six. We considered a connection from the j-th glial cell to the i-th neuron significant if the p-value of $t_{ij}^{N \leftarrow G}$ was smaller than 0.05 (marked with an asterisk).
(EPS)

Figure S4 Correlation between pairs of neurons and glial cells between which our method identified connections. (A) Our method detected a connection from neuron 6 to glial cell 1. Their activities actually exhibited a high correlation ($r = 0.80$, left panel). On the other hand, our method detected no connection from neuron 6 to glial cell 2. Their activities exhibited a lower correlation ($r = 0.53$, right panel). (B) The histogram of the cross correlation coefficient, r, indicates that the magnitude of the cross correlation between the activity pair of a glial cell and a neuron tends to be higher when there is an identified connection from the glial cell to the neuron. This claim could be statistically verified with the Wilcoxon rank sum test ($p < 0.01$). (C) The histogram of the cross correlation coefficient was not significantly different between connected neuron → glia pairs and non-connected neuron → glia pairs ($p = 0.10$, Wilcoxon rank sum test).
(EPS)

Figure S5 Detection of neuron-to-glia connections. Recall that $d_{ij}^{G \leftarrow N}$ is the loss in the cross-validated likelihood caused by the removal of the connection from the i-th neuron to the j-th glial cell, and $t_{ij}^{G \leftarrow N}$ is the t-statistics derived from $d_{ij}^{G \leftarrow N}$. The six panels summarize $t_{ij}^{G \leftarrow N}$ for all pairs of i and j. Each panel corresponds to a single glial cell (different index of j) out of the six. We considered a connection from the i-th neuron to the j-th glial cell significant if the p-value of $t_{ij}^{G \leftarrow N}$ was smaller than 0.05.
(EPS)

Figure S6 Length of identified neuron-to-glia and glia-to-neuron connections. Boxplots of the length of identified connections. The first, second, third, and fourth columns correspond to the sets of identified connections from glial cells to neurons ($\{N \leftarrow G\}$), identified connections from neurons to glial cells ($\{G \leftarrow N\}$), identified connections from neurons to glial cells by applying positivity constraints to the response functions ($\{G \leftarrow N\}_+$), and those in all neuron-glia pairs in the dataset ($\{Full\}$). The asterisk indicates that the median length of the identified glia-neuron connections was significantly shorter than those of the bootstrap samples (see Results in the main text) sampled from all the pairs $\{Full\}$ ($p < 0.05$).
(EPS)

Figure S7 Robustness against perturbation of smoothing parameters. The panel on the left indicates the average response functions from glial cells to neurons $b_{ij}(s)$ with different smoothing parameter values (red, blue, magenta, and green lines for $\lambda^{sm} = 0.1, 1, 10$, and 100, respectively). The panel on the right indicates the average response functions from neurons to glial cells $c_{ij}(s)$ with different smoothing parameter values (red, blue, magenta, and green lines for $\lambda^{sm} = 0.1, 1, 10$, and 100, respectively).
(EPS)

Figure S8 Correct rate (accuracy) in reconstruction of glia-to-neuron connections from artificial data. The error bars indicate the 95% confidence intervals of accuracy (50 trials).
(EPS)

Figure S9 Detection of neuron-to-glia connections by introducing positivity constraints to their response

functions. We implemented a modified version of our method with positivity constraints on the response functions from neurons to glia. Likewise in the original method, we used the t-statistic, $t_{ij}^{G \leftarrow N}$, to identify the connections. The modified method identified connections from some neurons to glia 2, 4, and 5 (marked in red). Under this new constraint, we could not detect any connection from neurons to glia 1, 3, and 6. The neurons indexed in green numerals in each panel indicate those with the identified connections to the glial cells marked red, whose removal degraded the cross-validated likelihood of the activity of the red-marked glial cells. The bottom right panel indicates the average for the estimated response functions of the identified neuron-to-glia connections, along with the 95% confidence interval at each delay time.
(EPS)

Table S1 Constraints on network structure for identification of neuron-to-glia connections (Eq. (1)).
(PDF)

Table S2 Constraints on network structure for identification of glia-to-neuron connections (Eq. (2)).
(PDF)

Table S3 Prior setting of model parameters.
(PDF)

Table S4 Tuning parameters and their constraints.
(PDF)

Text S1 Supplementary text. This text file describes the 'Iterative amplitude adjusted Fourier transform method', 'Validation of the proposed method using artificial data', and 'Comparison of network structures'.
(PDF)

Acknowledgments

Author Contributions

Conceived and designed the experiments: KN YI SI. Performed the experiments: TI YI. Analyzed the data: KN. Contributed reagents/materials/analysis tools: KN YI SO TI HU MK SI. Wrote the paper: KN YI SO TI HU MK SI.

References

1. Buzsaki G (2009) Rhythms of the brain. Oxford University Press.
2. Shepherd GM, et al. (2004) The synaptic organization of the brain, volume 4. Oxford University Press.
3. Hamilton NB, Attwell D (2010) Do astrocytes really exocytose neurotransmitters? Nat Rev Neurosci 11: 227–238.
4. Halassa MM, Haydon PG (2010) Integrated brain circuits: astrocytic networks modulate neuronal activity and behavior. Annu Rev Physiol 72: 335.
5. Henneberger C, Papouin T, Oliet SH, Rusakov DA (2010) Long-term potentiation depends on release of D-serine from astrocytes. Nature 463: 232–236.
6. Fellin T, Pascual O, Gobbo S, Pozzan T, Haydon PG, et al. (2004) Neuronal synchrony mediated by astrocytic glutamate through activation of extrasynaptic NMDA receptors. Neuron 43: 729–743.
7. Tian GF, Azmi H, Takano T, Xu Q, Peng W, et al. (2005) An astrocytic basis of epilepsy. Nat Med 11: 973–981.
8. Schipke CG, Kettenmann H (2004) Astrocyte responses to neuronal activity. Glia 47: 226–232.
9. Bernardinelli Y, Salmon C, Jones EV, Farmer WT, Stellwagen D, et al. (2011) Astrocytes display complex and localized calcium responses to single-neuron stimulation in the hippocampus. J Neurosci 31: 8905–8919.
10. Di Castro MA, Chuquet J, Liaudet N, Bhaukaurally K, Santello M, et al. (2011) Local Ca2+ detection and modulation of synaptic release by astrocytes. Nat Neurosci 14: 1276–1284.
11. Gordon GR, Iremonger KJ, Kantevari S, Ellis-Davies GC, MacVicar BA, et al. (2009) Astrocyte-mediated distributed plasticity at hypothalamic glutamate synapses. Neuron 64: 391–403.
12. Min R, Nevian T (2012) Astrocyte signaling controls spike timing-dependent depression at neocortical synapses. Nat Neurosci 15: 746–753.
13. Panatier A, Vallée J, Haber M, Murai KK, Lacaille JC, et al. (2011) Astrocytes are endogenous regulators of basal transmission at central synapses. Cell 146: 785–798.
14. Perea G, Araque A (2005) Properties of synaptically evoked astrocyte calcium signal reveal synaptic information processing by astrocytes. J Neurosci 25: 2192–2203.
15. Sofroniew MV, Vinters HV (2010) Astrocytes: biology and pathology. Acta Neuropathol (Berl) 119: 7–35.
16. Araque A, Parpura V, Sanzgiri RP, Haydon PG (1999) Tripartite synapses: glia, the unacknowledged partner. Trends Neurosci 22: 208–215.
17. Araque A, Sanzgiri RP, Parpura V, Haydon PG (1998) Calcium elevation in astrocytes causes an NMDA receptor-dependent increase in the frequency of miniature synaptic currents in cultured hippocampal neurons. J Neurosci 18: 6822–6829.
18. Volterra A, Meldolesi J (2005) Astrocytes, from brain glue to communication elements: the revolution continues. Nat Rev Neurosci 6: 626–640.
19. De Pittà M, Volman V, Berry H, Parpura V, Volterra A, et al. (2012) Computational quest for understanding the role of astrocyte signaling in synaptic transmission and plasticity. Front Comput Neurosci 6: 98
20. Schummers J, Yu H, Sur M (2008) Tuned responses of astrocytes and their influence on hemodynamic signals in the visual cortex. Science 320: 1638–1643.
21. Takata N, Mishima T, Hisatsune C, Nagai T, Ebisui E, et al. (2011) Astrocyte calcium signaling transforms cholinergic modulation to cortical plasticity in vivo. J Neurosci 31: 18155–18165.
22. Nimmerjahn A, Mukamel EA, Schnitzer MJ (2009) Motor behavior activates Bergmann glial networks. Neuron 62: 400–412.
23. Haydon PG (2001) GLIA: listening and talking to the synapse. Nat Rev Neurosci 2: 185–193.
24. Fields RD (2004) The other half of the brain. Sci Amer 290: 54–61.
25. Newman EA (2003) New roles for astrocytes: regulation of synaptic transmission. Trends Neurosci 26: 536–542.
26. Fields RD, Burnstock G (2006) Purinergic signalling in neuron–glia interactions. Nat Rev Neurosci 7: 423–436.
27. Gómez-Gonzalo M, Losi G, Chiavegato A, Zonta M, Cammarota M, et al. (2010) An excitatory loop with astrocytes contributes to drive neurons to seizure threshold. PLoS Biol 8: e1000352.
28. Okatan M, Wilson MA, Brown EN (2005) Analyzing functional connectivity using a network likelihood model of ensemble neural spiking activity. Neural Comput 17: 1927–1961.
29. Stevenson IH, Rebesco JM, Hatsopoulos NG, Haga Z, Miller LE, et al. (2009) Bayesian inference of functional connectivity and network structure from spikes. IEEE Tran Neural Syst Rehab Eng 17: 203–213.
30. Stevenson IH, London BM, Oby ER, Sachs NA, Reimer J, et al. (2012) Functional connectivity and tuning curves in populations of simultaneously recorded neurons. PLoS Comput Biol 8: e1002775.
31. Pillow JW, Shlens J, Paninski L, Sher A, Litke AM, et al. (2008) Spatio-temporal correlations and visual signalling in a complete neuronal population. Nature 454: 995–999.
32. Chen Z, Putrino DF, Ghosh S, Barbieri R, Brown EN (2011) Statistical inference for assessing functional connectivity of neuronal ensembles with sparse spiking data. Neural Systems and Rehabilitation Engineering, IEEE Transactions on 19: 121–135.
33. Kobayashi R, Kitano K (2013) Impact of network topology on inference of synaptic connectivity from multi-neuronal spike data simulated by a large-scale cortical network model. J Comput Neurosci 85: 1–16.
34. Friston K, Frith C, Liddle P, Frackowiak R (1993) Functional connectivity: the principal-component analysis of large (PET) data sets. J Cereb Blood Flow Metab 13: 5–5.
35. Valdes-Sosa PA, Roebroeck A, Daunizeau J, Friston K (2011) Effective connectivity: influence, causality and biophysical modeling. Neuroimage 58: 339–361.
36. Stetter O, Battaglia D, Soriano J, Geisel T (2012) Model-free reconstruction of excitatory neuronal connectivity from calcium imaging signals. PLoS Comput Biol 8: e1002653.
37. Constantinidis C, Williams GV, Goldman-Rakic PS (2002) A role for inhibition in shaping the temporal flow of information in prefrontal cortex. Nat Neurosci 5: 175–180.
38. Fujisawa S, Amarasingham A, Harrison MT, Buzsáki G (2008) Behavior-dependent short-term assembly dynamics in the medial prefrontal cortex. Nat Neurosci 11: 823–833.
39. Friston KJ (2011) Functional and effective connectivity: a review. Brain connectivity 1: 13–36.
40. Takahashi N, Sasaki T, Usami A, Matsuki N, Ikegaya Y (2007) Watching neuronal circuit dynamics through functional multineuron calcium imaging (fMCI). Neurosci Res 58: 219–225.

41. Kim S, Putrino D, Ghosh S, Brown EN (2011) A Granger causality measure for point process models of ensemble neural spiking activity. PLoS Comput Biol 7: e1001110.
42. Ikegaya Y, Sasaki T, Ishikawa D, Honma N, Tao K, et al. (2013) Interpyramid spike transmission stabilizes the sparseness of recurrent network activity. Cereb Cortex 23: 293–304.
43. Zorec R, Araque A, Carmignoto G, Haydon PG, Verkhratsky A, et al. (2012) Astroglial excitability and gliotransmission: an appraisal of Ca2+ as a signalling route. ASN neuro 4: AN20110061.
44. Bushong EA, Martone ME, Jones YZ, Ellisman MH (2002) Protoplasmic astrocytes in CA1 stratum radiatum occupy separate anatomical domains. J Neurosci 22: 183–192.
45. Halassa MM, Fellin T, Takano H, Dong JH, Haydon PG (2007) Synaptic islands defined by the territory of a single astrocyte. J Neurosci 27: 6473–6477.
46. Wilhelmsson U, Bushong EA, Price DL, Smarr BL, Phung V, et al. (2006) Redefining the concept of reactive astrocytes as cells that remain within their unique domains upon reaction to injury. Proc Natl Acad Sci U S A 103: 17513–17518.
47. Angulo MC, Kozlov AS, Charpak S, Audinat E (2004) Glutamate released from glial cells synchronizes neuronal activity in the hippocampus. J Neurosci 24: 6920–6927.
48. Sasaki T, Kuga N, Namiki S, Matsuki N, Ikegaya Y (2011) Locally synchronized astrocytes. Cereb Cortex 21: 1889–1900.
49. Newman EA (2005) Calcium increases in retinal glial cells evoked by light-induced neuronal activity. J Neurosci 25: 5502–5510.
50. Dani JW, Chernjavsky A, Smith SJ (1992) Neuronal activity triggers calcium waves in hippocampal astrocyte networks. Neuron 8: 429–440.
51. Haustein MD, Kracun S, Lu XH, Shih T, Jackson-Weaver O, et al. (2014) Conditions and constraints for astrocyte calcium signaling in the hippocampal mossy fiber pathway. Neuron 82: 413–429.
52. Zhang Q, Haydon P (2005) Roles for gliotransmission in the nervous system. J Neural Transm 112: 121–125.
53. Wang DD, Bordey A (2008) The astrocyte odyssey. Prog Neurobiol 86: 342–367.
54. Chesler M (2003) Regulation and modulation of pH in the brain. Physiol Rev 83: 1183–1221.
55. Cengiz P, Kintner DB, Chanana V, Yuan H, Akture E, et al. (2014) Sustained Na+/H+ exchanger activation promotes gliotransmitter release from reactive hippocampal astrocytes following oxygen-glucose deprivation. PLoS One 9: e84294.
56. Matyash V, Kettenmann H (2010) Heterogeneity in astrocyte morphology and physiology. Brain Res Brain Res Rev 63: 2–10.
57. Shadlen MN, Newsome WT (1994) Noise, neural codes and cortical organization. Curr Opin Neurobiol 4: 569–579.
58. Shadlen MN, Newsome WT (1998) The variable discharge of cortical neurons: implications for connectivity, computation, and information coding. J Neurosci 18: 3870–3896.
59. Granger CW (1969) Investigating causal relations by econometric models and cross-spectral methods. Econometrica 85: 424–438.
60. Lungarella M, Ishiguro K, Kuniyoshi Y, Otsu N (2007) Methods for quantifying the causal structure of bivariate time series. Int J Bifurcat Chaos 17: 903–921.
61. Mishchenko Y, Vogelstein JT, Paninski L (2011) A Bayesian approach for inferring neuronal connectivity from calcium fluorescent imaging data. Ann Appl Stat 5: 1229–1261.
62. Geweke JF (1984) Measures of conditional linear dependence and feedback between time series. J Am Stat Assoc 79: 907–915.
63. Hamilton JD (1994) Time series analysis, volume 2. Princeton university press Princeton.
64. Chklovskii DB, Vitaladevuni S, Scheffer LK (2010) Semi-automated reconstruction of neural circuits using electron microscopy. Curr Opin Neurobiol 20: 667–675.
65. Tang A, Jackson D, Hobbs J, Chen W, Smith JL, et al. (2008) A maximum entropy model applied to spatial and temporal correlations from cortical networks in vitro. J Neurosci 28: 505–518.
66. Shimazaki H, Amari Si, Brown EN, Grün S (2012) State-space analysis of time-varying higher-order spike correlation for multiple neural spike train data. PLoS Comput Biol 8: e1002385.
67. Grün S (2009) Data-driven significance estimation for precise spike correlation. J Neurophysiol 101: 1126–1140.
68. Sasaki T, Matsuki N, Ikegaya Y (2007) Metastability of active CA3 networks. J Neurosci 27: 517–528.
69. Takahashi N, Oba S, Yukinawa N, Ujita S, Mizunuma M, et al. (2011) High-speed multineuron calcium imaging using Nipkow-type confocal microscopy. Curr Protoc Neurosci 2: 1–10.
70. Zhao M, Batista A, Cunningham JP, Chestek C, Rivera-Alvidrez Z, et al. (2012) An L 1-regularized logistic model for detecting short-term neuronal interactions. J Comput Neurosci 32: 479–497.
71. Wahba G (1990) Spline models for observational data. Society for Industrial Mathematics.
72. Bishop CM, Nasrabadi NM (2006) Pattern recognition and machine learning, volume 1. Springer New York.
73. Byrd RH, Lu P, Nocedal J, Zhu C (1995) A limited memory algorithm for bound constrained optimization. SIAM J Sci Comput 16: 1190–1208.
74. Schreiber T (2000) Measuring information transfer. Phys Rev Lett 85: 461.
75. Louis S, Gerstein GL, Grün S, Diesmann M (2010) Surrogate spike train generation through dithering in operational time. Front Comput Neurosci 4.
76. Wright S, Nocedal J (1999) Numerical optimization, volume 2. Springer New York.

Sound-induced modulation of hippocampal θ oscillations

Reimi Abe[a,*], Tetsuya Sakaguchi[a,*], Keiichi Kitajo[b], Daisuke Ishikawa[a], Nobuyoshi Matsumoto[a], Norio Matsuki[a] and Yuji Ikegaya[a,c]

The mechanism of response of hippocampal neurons to a specific feature in sensory stimuli is not fully understood, although the hippocampus is well known to contribute to the formation of episodic memory in the multisensory world. Using in-vivo voltage-clamp recordings from awake mice, we found that sound pulses induced a transient increase in inhibitory, but not excitatory, conductance in hippocampal CA1 pyramidal cells. In local field potentials, sound pulses induced a phase resetting of the θ oscillations, one of the major oscillatory states of the hippocampus. Repetitive sound pulses at 7 Hz (θ rhythm) increased the θ oscillation power, an effect that was abolished by a surgical fimbria–fornix lesion. Thus, tone-induced inhibition is likely of subcortical origin. It may segment hippocampal neural processing and render temporal boundaries in continuously ongoing experiences. *NeuroReport* 25:1368–1374 © 2014 Wolters Kluwer Health | Lippincott Williams & Wilkins.

Introduction

The hippocampus plays a role in encoding snapshots during daily life experiences and creating episodic memory [1]. One of the major network oscillations of the hippocampus is θ-rhythm (4–12 Hz) oscillations, which are likely to represent a memory-encoding state [2]. Indeed, the θ oscillation power correlates positively with the cognitive ability of animals [3] and humans [4,5]. In rodents, hippocampal neurons modulate their firing patterns depending on the location of the animal and collectively generate a cognitive map of space [6], and these firing patterns are modulated by θ rhythm [7]. Such internal representations regarding behavioral experience emerge and are updated through visual, auditory, olfactory, gustatory, and somatosensory information. In the present work, we investigated the effect of auditory stimuli to hippocampal θ field oscillations in awake mice. To this end, we first sought to examine how individual hippocampal neurons respond to sound, using in-vivo whole-cell patch-clamp recordings from CA1 pyramidal cells, because there is little literature about the intracellular responses of hippocampal neurons to sound in awake mice. We report here that auditory stimuli induce a transient inhibitory input to CA1 neurons and a phase resetting of θ field oscillations. Moreover, θ-rhythm tone pulses increase the θ oscillation power.

Methods

Animal ethics

The experiments were performed with the approval of the animal experiment ethics committee at the University of Tokyo (approval number: P26-5) and according to the NIH guidelines for the care and use of animals. Male ICR mice (21–45 days old) were housed in cages under standard laboratory conditions (12 h light/dark cycle) and had access to water and food *ad libitum*.

Surgery

Mice were anesthetized with ketamine (50 mg/kg, intraperitoneal) and xylazine (10 mg/kg, intraperitoneal) and were implanted with a metal head-holding plate weighing 175 mg [8,9]. After recovery, the mice were subjected to head-fixation training on a custom-made stereotaxic fixture. Training was repeated for 1–3 h/day until the implanted animal learned to remain quiet. The animal was rewarded with free access to sucrose-containing water during training, although the consumption amount of sucrose seemed unlikely to correlate with the success rate of habituation. Full habituation usually required 5–10 consecutive days. Then, the mice were anesthetized with a ketamine/xylazine cocktail and were craniotomized (1 × 1 mm²), centered at 2.2 mm posterior and 2.0 mm lateral to the bregma for recordings from CA1, or at 3.8 mm posterior and 3–3.8 mm lateral to the bregma for recordings from the entorhinal cortex. The dura was surgically removed, and the exposed brain tissue surface was covered with 1.7% agar. Throughout the experiments, a heating pad maintained the rectal temperature at 37°C, and the surgical region was analgesized with 0.2% lidocaine. After the mice recovered from the anesthesia, recordings were made under head fixation in a sound-proof box. In experiments shown in Fig. 3b, the fimbria–fornix (FF) tract was bilaterally transected before recording. A retractable knife (~4 mm in width) was

lowered to 3 mm depth from the cortex surface through a small burr hole in the skull (0.5 mm posterior, ±2.2 mm lateral to the bregma) under stereotactic guidance. As auditory stimuli, sine-wave pure tones (duration: 10–300 ms; frequency: 4 kHz; intensity: 70–110 dB) were applied at an interval of 6–16 s from a speaker placed in front of the mice (25 cm away from the nose). In each block, tones with different conditions were presented in a random order.

Electrophysiology

Patch-clamp recordings were obtained from neurons in the CA1 stratum pyramidale (AP: −2.0 mm; ML: 2.0 mm; DV: 1.1–1.3 mm) using borosilicate glass electrodes (4–7 MΩ). Pyramidal cells were identified by their regular spiking properties and by post-hoc histological analysis. The intrapipette solution consisted of the following reagents (in mM): 140 Cs-methanesulfonate, 5 HEPES, 10 TEA-Cl, 1 EGTA, 10 Na_2-phosphocreatine, 1 MgATP (pH 7.2), and 0.2% biocytin. Sound-evoked excitatory and inhibitory postsynaptic conductances (EPSGs and IPSGs) were measured at clamped voltages of −70 and 0 mV, respectively [8, 10]. Experiments in which the series resistance exceeded 70 MΩ or changed by more than 15% during the entire recording session were discarded. For local field potential (LFP) recordings, the pipettes (1.5–3.5 MΩ) were filled with artificial cerebrospinal fluid, which consisted of the following reagents (in mM): 127 NaCl, 1.6 KCl, 1.24 KH_2PO_4, 1.3 $MgSO_4$, 2.4 $CaCl_2$, 26 $NaHCO_3$, and 10 glucose. LFPs were recorded from hippocampal CA1 stratum pyramidale, radiatum, or lacunosum moleculare (AP: −2.0 mm; ML: 2.0 mm; DV: 1.1–1.4 mm) or entorhinal cortex (AP: −4.0 mm; ML: 3.2 mm; DV: 1.4–1.5 mm). For recordings form entorhinal cortex, the electrodes were inserted at an angle of 8–10° in the sagital plane with the tip pointing in the posterior direction. The signals were amplified and digitized at a sampling rate of 20 kHz using a MultiClamp 700B amplifier (Molecular Devices, California, USA) and a Digidata 1440A digitizer (Molecular Devices) that were controlled by pCLAMP 10.3 software (Molecular Devices). Data were analyzed off-line using custom-made MATLAB (R2012b; MathWorks, Natick, Massachusetts, USA) routines.

Histology

After each recording, the biocytin-containing pipette was carefully removed from the brain, and the mice were anesthetized with an overdose of urethane. After they were completely anesthetized, they were perfused transcardially with chilled PBS, followed by 4% paraformaldehyde in 0.1 M PBS (pH 7.4). The brains were removed and stored overnight at 4°C in a 4% paraformaldehyde solution. Then they were coronally sectioned at a thickness of 100 μm. The sections were incubated with 0.3% H_2O_2 for 30 min. After permeabilization in 0.2% Triton X-100 for 1 h, they were processed with ABC reagent at 4°C overnight and with 0.0003%

H_2O_2, 0.02% diaminobenzidine, and 10 mM $(NH_4)_2Ni$ $(SO_4)_2$. The success rate for reconstruction of the recoded neurons was ∼80% and depended on the durations and qualities of the recordings. We did not find a leaky staining of biocytin that may occur because of approach to the cells with intrapipette pressures.

Results

Tone-induced increase in inhibitory conductance of hippocampal CA1 neurons

Pyramidal cells were patch-clamped from the CA1 area of awake, head-fixed mice (Fig. 1a), and the mice were given 4-kHz sine-wave pure tones for 30 ms. The neurons were voltage-clamped, and excitatory and inhibitory synaptic currents were isolated. Tone stimulation induced a rapid and transient increase in IPSGs without an apparent change in EPSGs (Fig. 1b; $n = 8$ neurons from eight mice, 10–50 trials each). The transient IPSGs were consistently observed in all eight neurons recorded; the mean peak amplitude of IPSGs was 0.45 ± 0.12 nS, and the peak latency was 63.8 ± 3.1 ms after the tone onset (mean ± SEM of eight neurons). The peak amplitude of IPSGs increased with tone intensities (Fig. 1c; $n = 3$ neurons from three mice, 10–20 trials each).

Tone-induced phase resetting and entrainment of θ field oscillations

Because phasic inhibitory inputs are known to modulate oscillatory neuronal activity [11,12], we examined the effect of tone stimuli on hippocampal LFP oscillations. Mice were given 4-kHz tones for 300 ms, while LFPs were recorded from the CA1 stratum pyramidale, radiatum, or lacunosum moleculare (Fig. 2a). We first conducted a cross-correlation analysis to assess the trial-to-trial variability (Fig. 2b and c). The across-trial correlation coefficients were calculated for various time periods (Fig. 2a; bottom). They exhibited the highest peak for 1 s after the tone onset (Fig. 2b and c; $n = 17$ mice, **$P < 0.01$, Dunnett's test), suggesting that hippocampal neurons were phasically synchronized by tone stimuli. We focused on the fluctuation of θ rhythm oscillations, one of the major hippocampal network oscillations. For each trial, Fast Fourier Transform analyses of LFPs revealed that a single-pulse tone stimulus did not induce a significant change in the power of θ field oscillations; the change ratio of the θ power (4–12 Hz) during the 3-s period after the tone onset to before the tone onset was -0.05 ± 0.06 (mean ± SEM of 17 mice, $P = 0.41$, $t_{16} = 0.84$, paired t-test). However, in the stimulus-triggered average of the LFP traces, the θ power was significantly enhanced by tone stimulation; the change ratio was 1.42 ± 0.39 (mean ± SEM of 17 mice, $P = 0.002$, $t_{16} = 3.6$, paired t-test). Moreover, we found that tone stimuli forced θ oscillations into the identical phase, irrespective of the instantaneous phase at the stimulation onset time (Fig. 2d). Rayleigh's phase analysis [13] indicated that the phase congruity persisted for ∼400 ms

Fig. 1
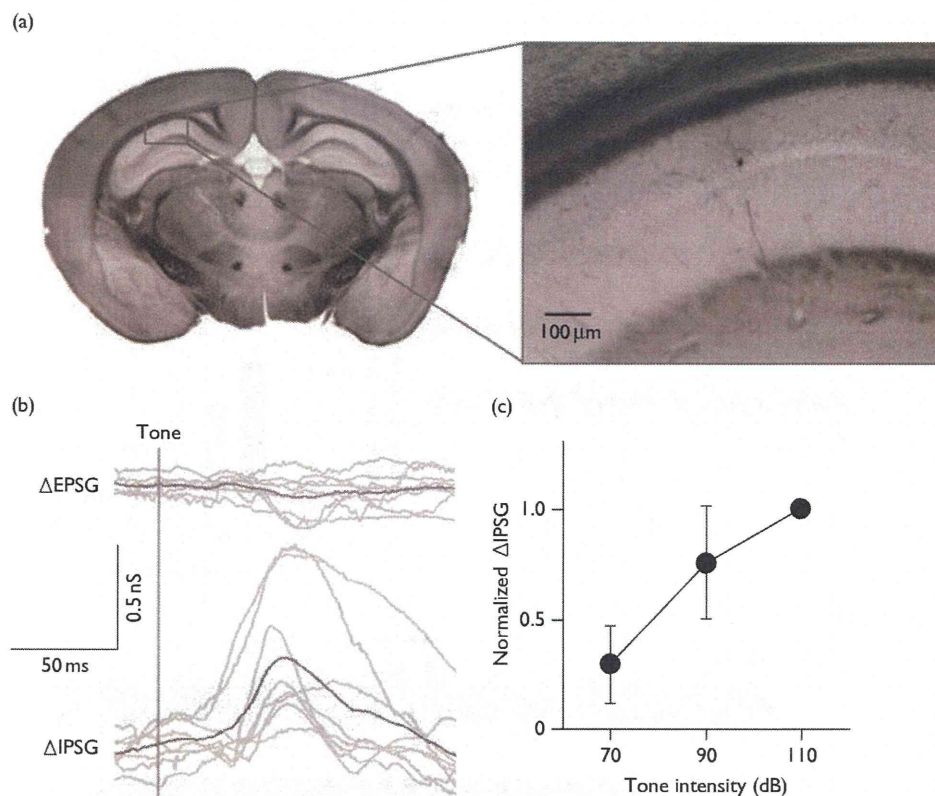
Tone-induced increase in inhibitory conductance of hippocampal CA1 neurons. (a) Biocytin reconstruction of an in-vivo whole-cell recorded CA1 pyramidal cell. (b) The mean traces of EPSGs and IPSGs in response to sound stimuli (gray bar: 30 ms, 4 kHz, 110 dB). Gray lines indicate eight individual cells from eight mice. For each cell, all traces observed (10–50 trials each) were averaged. The black lines indicate the averages of the eight cells. (c) The peak amplitude of ΔIPSG depended on the tone intensity. The error bars are SEMs of three cells from three mice. EPSG, excitatory postsynaptic conductance; IPSG, inhibitory postsynaptic conductance.

(Fig. 2d, bottom). In a total of 405 tone-stimulus trials pooled from LFPs in the CA1 in 17 mice, the phase distributions of θ oscillations at − 1000 and 150 ms relative to the tone onset showed that the initially uniform phase distribution was biased 150 ms after tone stimulation (Fig. 2e; $P = 1.3 \times 10^{-48}$, Rayleigh's $Z = 110$, Rayleigh's test for circular uniformity), indicating that tone-induced phase resetting is consistent across trials and animals. The same phase analyses were repeated for different oscillation frequencies at 150 ms after the tone onset (Fig. 2f). Rayleigh's Z spectrum was peaked at around 7 Hz, suggesting that tone-induced phase reset is specific to the θ oscillation range.

The rodent hippocampus and the entorhinal cortex may emit synchronized oscillations [14,15]. Indeed, we found that tone induced a θ phase resetting in the entorhinal cortex (Fig. 2e; $P = 2.5 \times 10^{-19}$, Rayleigh's $Z = 42.8$ at 150 ms after the tone onset). However, the increase in Rayleigh's Z scores was not specific to the θ band, and the increased level was lower than that in CA1 (Fig. 2f).

Therefore, the LFP modulations in the entorhinal cortex cannot fully account for the CA1 θ resetting.

θ-Frequency stimulation of the hippocampal inhibitory network is reported to synchronize principal cells [16,17]. We next applied repetitive tone stimulation at a θ frequency of 7 Hz. The 7-Hz stimulation with 20-ms tone pulses for 5 s increased the θ power in the CA1 stratum pyramidale (Fig. 3a). This power enhancement was not observed for oscillation frequencies other than 7 Hz (Fig. 3b; right). Interestingly, the 7-Hz stimulation significantly reduced the 2-Hz power. Thus, hippocampal oscillations seemed to interact across frequencies. Therefore, we examined whether θ oscillations are induced by other stimulation frequencies. Tone pulses were repeated for 5 s at 2, 7, 20, and 50 Hz. The θ resonance was induced by 7-Hz stimulation but not by 2-, 20-, or 50-Hz stimulation (Fig. 3c). Incidentally, 2-Hz stimulation enhanced the 2-Hz oscillation power, whereas neither 20- nor 50-Hz stimulation altered the 20- or 50-Hz oscillation powers, respectively (Fig. 3d).

Fig. 2
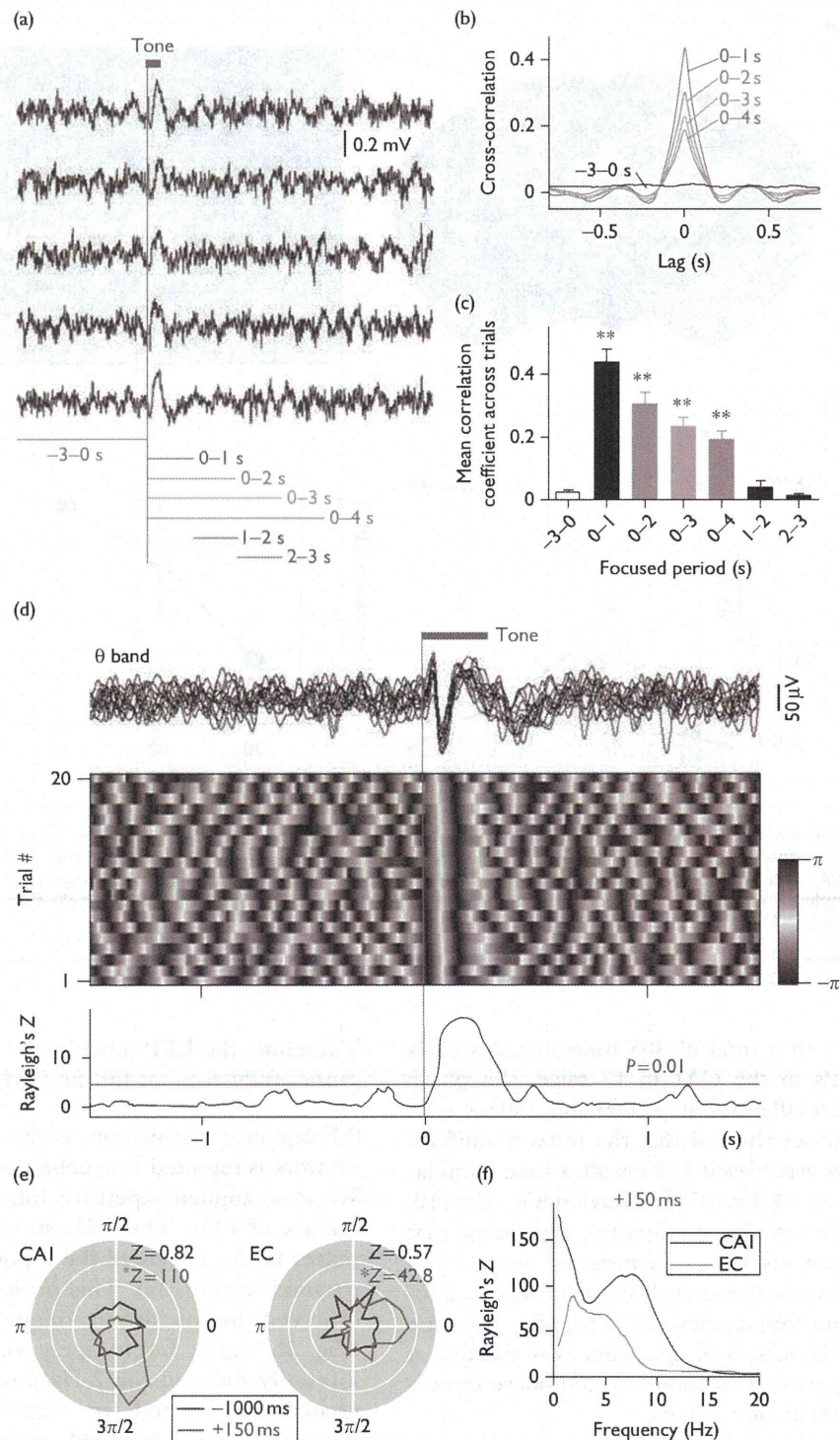
Tone-induced θ phase reset. (a) Representative local field potential (LFP) responses to the tones (gray bar: 300 ms, 4 kHz, 110 dB) were recorded from CA1 stratum pyramidale. (b) The mean cross-correlograms across all possible pairs of the trials were obtained for various time periods indicated in (a) ($n = 17$ mice). Data recorded from the CA1 stratum pyramidale, radiatum, or lacunosum moleculare were pooled. (c) The mean correlation coefficients in (b) (mean ± SEM of 17 mice, **$P < 0.01$, Dunnett's test). (d) Representative LFP traces filtered in a band of 5–10 Hz (all 20 sweeps, top), their θ-phase pseudocolored map (middle), and their Rayleigh's Z score (bottom). The data were recorded from the CA1 stratum pyramidale. (e) Distributions of the phases of 7-Hz oscillations in the CA1 and the entorhinal cortex (EC) at −1000 and 150 ms after the tone onset. The data were pooled from a total of 405 trials in 17 mice for CA1 (−1000 ms: $P = 0.44$, $Z = 0.82$; +150 ms: $P = 1.3 \times 10^{-48}$, $Z = 110$, Rayleigh's test for circular uniformity) and from a total of 170 trials in five mice for EC (−1000 ms: $P = 0.56$, $Z = 0.58$; +150 ms: $P = 2.5 \times 10^{-19}$, $Z = 42.8$). (f) Rayleigh's Z spectra of CA1 and EC LFPs at 150 ms after the tone onset (CA1: $n = 17$ mice, EC: $n = 5$ mice).

Fig. 3
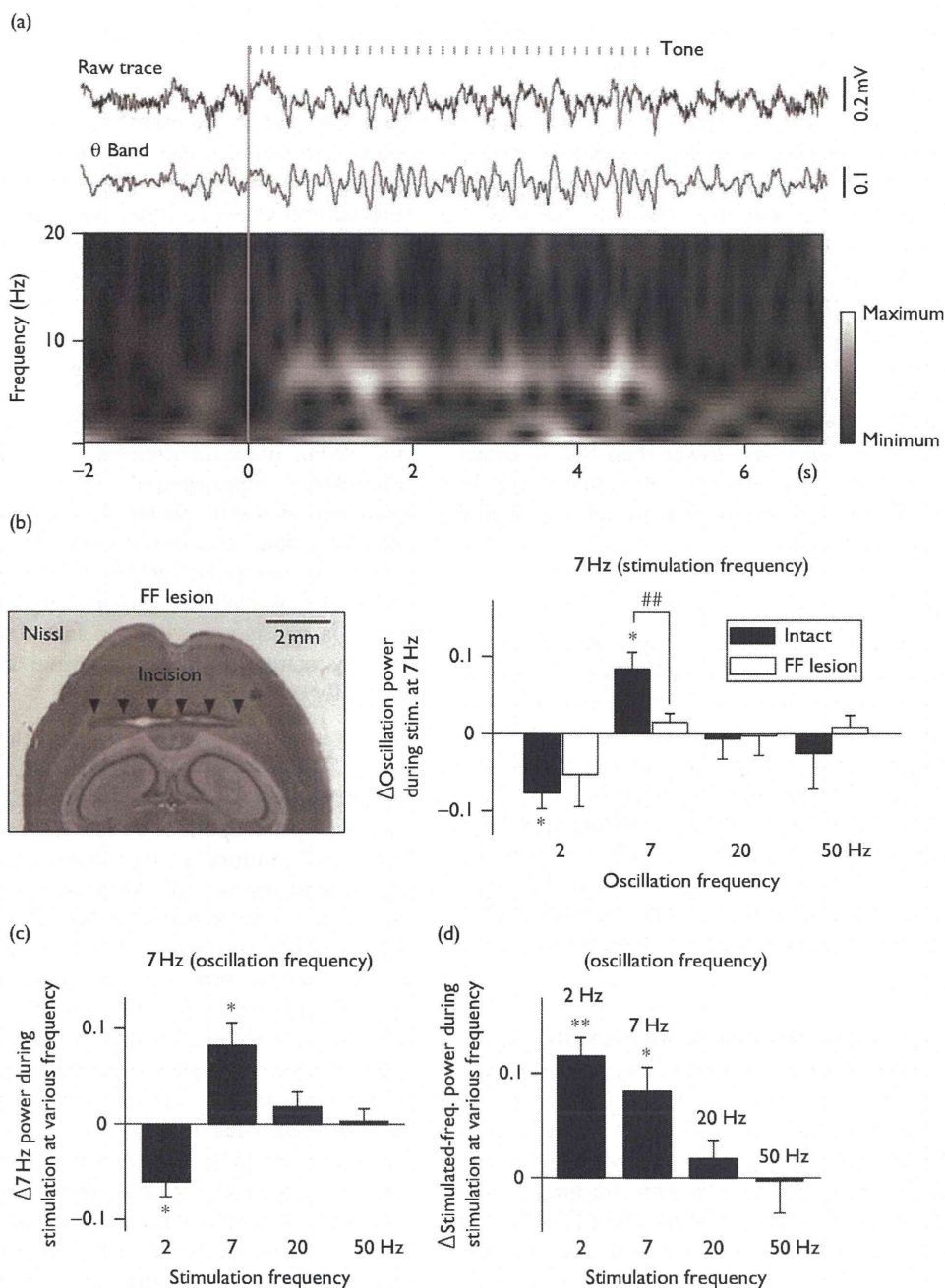
Tone-induced θ resonance in the CA1 stratum pyramidale. (a) Typical raw and 4–12-Hz band filtered traces of local field potential (LFP) recorded from CA1 stratum pyramidale and the wavelet-based power spectrum of the raw LFP in response to 110-dB tone stimulation at 7 Hz. (b) Left: a representative Nissl-stained horizontal section of the brain in a fimbria–fornix (FF)-lesioned mouse. Right: tone stimulation at 7 Hz selectively enhanced the 7-Hz oscillation power in the LFPs in intact mice but not in FF-lesioned mice. The oscillation powers were compared as the ratio of the 3-s period (2–5 s) after the tone onset to the control period (0–3 s) before the tone onset (2 Hz: *$P = 0.017$, $t_5 = 3.53$; 7 Hz: *$P = 0.018$, $t_5 = 3.47$, paired t-test, ##$P < 0.01$, Duncan's test, $n = 6$ mice for intact and four mice for FF lesion). (c) Tone-induced changes in the θ power at stimulation frequencies of 2, 7, 20, and 50 Hz (2 Hz: *$P = 0.016$, $t_5 = 3.58$; 7 Hz: *$P = 0.018$, $t_5 = 3.47$, $n = 6$ mice). (d) Tone-induced changes in the power of each oscillation frequency at the corresponding stimulation frequency (2 Hz: **$P = 1.2 \times 10^{-3}$, $t_5 = 6.56$; 7 Hz: *$P = 0.018$, $t_5 = 3.47$, $n = 6$ mice). The error bars are SEMs.

Lack of tone-induced θ entrainment in fimbria–fornix-lesioned mice

The major afferents to the hippocampus are supplied through the temporoammonic pathway from the entorhinal cortex and the FF pathway from subcortical areas. Medial septal neurons, which project to the hippocampus through FF fibers, increase their firing rates in response to various sensory stimuli, including sound, touch, and light [18,19]. An imaging study demonstrated that medial septal GABAergic fibers projecting to CA1 stratum oriens respond to sensory inputs with transient calcium elevations [20]. Moreover, recent works indicate that repetitive stimulation of septal GABAergic neurons induces θ-rhythm oscillations in hippocampal LFPs [16,17]. We thus applied tone stimuli to mice in which the FF was surgically transected (Fig. 3b; left). The baseline θ power in these FF-lesioned mice was lower than that in intact mice (data not shown), as reported previously [21]. In these mice, CA1 neurons did not exhibit tone-induced θ resonance (Fig. 3b; right).

Discussion

Information about the intracellular responses of hippocampal neurons to sensory inputs is still sparse, and, to the best of our knowledge, previous studies were all conducted under anesthesia. In urethane-anesthetized rats, for example, hippocampal CA1 neurons exhibit a long-delayed hyperpolarization in response to somatosensory stimuli [22,23] and θ-rhythm membrane potential fluctuations after tail pinch stimulation [22]. Using awake mice, we demonstrated that CA1 pyramidal cells responded to the onset of a sound with a transient IPSG. We also found that sound induced a θ phase resetting and θ resonance.

Inhibitory input through the fimbria–fornix pathway

The hippocampus receives both excitatory and inhibitory projections through the FF pathway. Medial septal neurons are known to fire in response to various sensory stimuli [18,19,24]. Indeed, a previous report showed that hippocampal GABAergic afferents from the medial septum are responsive to auditory stimulation [20] and that repetitive stimulation of these axons induces θ field oscillations [16,17]. Thus, the medial septum is a candidate brain area that mediates sound-induced IPSGs in the hippocampus, although our data do not exclude the involvement of other subcortical regions.

The septohippocampal GABAergic terminals make synapses predominantly with inhibitory interneurons in the hippocampus [25] and are presumed to enhance hippocampal network excitability through disynaptic disinhibition. In contrast to this expectation, we observed that sound induced IPSGs, but not EPSGs (Fig. 1b). Besides GABAergic projections, however, previous investigations have demonstrated that the medial septum sends cholinergic and glutamatergic fibers to the hippocampus [26,27]. These excitatory inputs may activate hippocampal interneurons and thereby elicit a hippocampal network suppression.

Tone-induced phase resetting and inhibitory input

Phasic inhibition is reported to modulate hippocampal θ oscillations [11,12]. For instance, stimulation of a CA1 interneuron evokes a hyperpolarization of a postsynaptic CA1 pyramidal cell and resets its intrinsic rhythmic state [12]. Therefore, tone-evoked IPSGs may serve to reset the intrinsic oscillation phase of individual pyramidal cells and thereby synchronize neuronal activities. We found that repetitive tone pulses at 7 Hz increased the θ oscillation power (Fig. 3). Likewise, 2-Hz tone pulses increased the δ (2 Hz) oscillation power, but neither 20- nor 50-Hz pulses entrained the oscillations (Fig. 3d). Therefore, hippocampal networks may be easily entrained at the θ and the δ frequencies through rhythmic activation of interneurons [12,28,29]. In contrast, repetitive tone pulses at 2 and 7 Hz decreased the power of θ and δ oscillations, respectively (Fig. 3b and c). This result is consistent with the fact that the rhythmical θ activity state and the slow-wave δ activity state are mutually exclusive [2].

Sound stimuli consistently shifted the θ phase to a fixed angle. Thus, the phase resetting does not depend on the instantaneous neural state of the hippocampus. During hippocampus-dependent tasks, sensory stimuli are reported to induce a phase resetting of θ oscillations in the dentate gyrus [30]. Moreover, previous reports suggest that phase resetting induces appropriate dynamics for encoding and retrieval of memory [31]. The tone-induced phase resetting in the hippocampus and the entorhinal cortex may also contribute to cognitive processes by synchronizing ongoing oscillations in these two regions. Recent evidence indicates that place cell activities switch along θ cycles with environmental contexts [32] and that their repeated θ sequences are segmented by landmarks [33]. These findings suggest that θ cycles are a functional unit that represents the environment in segments. We speculate that sensory-evoked inhibitory inputs contribute to temporal segmentation of hippocampal neural processing and therefore the cognitive chunking of continuously ongoing experiences.

Acknowledgements

Conflicts of interest

There are no conflicts of interest.

References

1 Scoville WB, Milner B. Loss of recent memory after bilateral hippocampal lesions. *J Neurol Neurosurg Psychiatry* 1957; **20**:11–21.

2 Buzsáki G. Two-stage model of memory trace formation: a role for 'noisy' brain states. *Neuroscience* 1989; **31**:551–570.

3 Buzsáki G. Neural syntax: cell assemblies, synapsembles, and readers. *Neuron* 2010; **68**:362–385.

4 Guderian S, Schott BH, Richardson-Klavehn A, Düzel E. Medial temporal theta state before an event predicts episodic encoding success in humans. *Proc Natl Acad Sci USA* 2009; **106**:5365–5370.

5 Gasser T, Möcks J, Lenard HG, Bächer P, Verleger R. The EEG of mildly retarded children: developmental, classificatory, and topographic aspects. *Electroencephalogr Clin Neurophysiol* 1983; **55**:131–144.

6 O'Keefe J, Dostrovsky J. The hippocampus as a spatial map. Preliminary evidence from unit activity in the freely-moving rat. *Brain Res* 1971; **34**:171–175.

7 Harvey CD, Collman F, Dombeck DA, Tank DW. Intracellular dynamics of hippocampal place cells during virtual navigation. *Nature* 2009; **461**:941–946.

8 Ishikawa D, Matsumoto N, Sakaguchi T, Matsuki N, Ikegaya Y. Operant conditioning of synaptic and spiking activity patterns in single hippocampal neurons. *J Neurosci* 2014; **34**:5044–5053.

9 Abe R, Sakaguchi T, Matsumoto N, Matsuki N, Ikegaya Y. Sound-induced hyperpolarization of hippocampal neurons. *Neuroreport* 2014; **25**:1013–1017.

10 Mizunuma M, Norimoto H, Tao K, Egawa T, Hanaoka K, Sakaguchi T, *et al.* Unbalanced excitability underlies offline reactivation of behaviorally activated neurons. *Nat Neurosci* 2014; **17**:503–505.

11 Ermentrout B. Type I membranes, phase resetting curves, and synchrony. *Neural Comput* 1996; **8**:979–1001.

12 Cobb SR, Buhl EH, Halasy K, Paulsen O, Somogyi P. Synchronization of neuronal activity in hippocampus by individual GABAergic interneurons. *Nature* 1995; **378**:75–78.

13 Kawasaki M, Uno Y, Mori J, Kobata K, Kitajo K. Transcranial magnetic stimulation-induced global propagation of transient phase resetting associated with directional information flow. *Front Hum Neurosci* 2014; **8**:173.

14 Mizuseki K, Sirota A, Pastalkova E, Buzsáki G. Theta oscillations provide temporal windows for local circuit computation in the entorhinal–hippocampal loop. *Neuron* 2009; **64**:267–280.

15 Colgin LL, Denninger T, Fyhn M, Hafting T, Bonnevie T, Jensen O, *et al.* Frequency of gamma oscillations routes flow of information in the hippocampus. *Nature* 2009; **462**:353–357.

16 Ducharme G, Amilhon B, Glasgow S, Adamantidis DA, Williams S. Modulation of hippocampal theta rhythm by optogenetic control of GABAergic projections from the medial septum [abstract]. *Soc Neurosci* 2013; **132**:06.

17 Justus D, Fuhrmann F, Kaneko H, Friedrichs D, Beutel T, Schoch S, *et al.* Optogenetic pacemaking of hippocampal oscillations in awake behaving mice [abstract]. *Soc Neurosci* 2013; **425**:20.

18 Mercer LF Jr, Remley NR. Mapping of sensory-responsive cells in the septal area of the rat. *Brain Res Bull* 1979; **4**:483–490.

19 Zhang H, Lin SC, Nicolelis MA. A distinctive subpopulation of medial septal slow-firing neurons promote hippocampal activation and theta oscillations. *J Neurophysiol* 2011; **106**:2749–2763.

20 Kaifosh P, Lovett-Barron M, Turi GF, Reardon TR, Losonczy A. Septo-hippocampal GABAergic signaling across multiple modalities in awake mice. *Nat Neurosci* 2013; **16**:1182–1184.

21 Lipponen A, Woldemichael BT, Gurevicius K, Tanila H. Artificial theta stimulation impairs encoding of contextual fear memory. *PLoS One* 2012; **7**:e48506.

22 Kamondi A, Acsády L, Wang XJ, Buzsáki G. Theta oscillations in somata and dendrites of hippocampal pyramidal cells in vivo: activity-dependent phase-precession of action potentials. *Hippocampus* 1998; **8**:244–261.

23 Bellistri E, Aguilar J, Brotons-Mas JR, Foffani G, de la Prida LM. Basic properties of somatosensory-evoked responses in the dorsal hippocampus of the rat. *J Physiol* 2013; **591**:2667–2686.

24 Brankack J, Buzsáki G. Hippocampal responses evoked by tooth pulp and acoustic stimulation: depth profiles and effect of behavior. *Brain Res* 1986; **378**:303–314.

25 Amaral D, Lavanex P. Hippocampal neuroanatomy. In: Andersen PMR, Amaral D, Bliss T, O'Keefe J, editors. *The hippocampus book*. Oxford, New York: Oxford University Press; 2007. pp. 37–114.

26 Lovett-Barron M, Kaifosh P, Kheirbek MA, Danielson N, Zaremba JD, Reardon TR, *et al.* Dendritic inhibition in the hippocampus supports fear learning. *Science* 2014; **343**:857–863.

27 Huh CY, Goutagny R, Williams S. Glutamatergic neurons of the mouse medial septum and diagonal band of Broca synaptically drive hippocampal pyramidal cells: relevance for hippocampal theta rhythm. *J Neurosci* 2010; **30**:15951–15961.

28 Melzer S, Michael M, Caputi A, Eliava M, Fuchs EC, Whittington MA, *et al.* Long-range-projecting GABAergic neurons modulate inhibition in hippocampus and entorhinal cortex. *Science* 2012; **335**:1506–1510.

29 Stark E, Eichler R, Roux L, Fujisawa S, Rotstein HG, Buzsáki G. Inhibition-induced theta resonance in cortical circuits. *Neuron* 2013; **80**:1263–1276.

30 Givens B. Stimulus-evoked resetting of the dentate theta rhythm: relation to working memory. *Neuroreport* 1996; **8**:159–163.

31 Hasselmo ME, Stern CE. Theta rhythm and the encoding and retrieval of space and time. *Neuroimage* 2014; **85 (Pt 2)**:656–666.

32 Jezek K, Henriksen EJ, Treves A, Moser EI, Moser MB. Theta-paced flickering between place-cell maps in the hippocampus. *Nature* 2011; **478**:246–249.

33 Gupta AS, van der Meer MA, Touretzky DS, Redish AD. Segmentation of spatial experience by hippocampal theta sequences. *Nat Neurosci* 2012; **15**:1032–1039.

ORIGINAL PAPER

Ex vivo cultured neuronal networks emit in vivo-like spontaneous activity

Kazuki Okamoto · Tomoe Ishikawa · Reimi Abe ·
Daisuke Ishikawa · Chiaki Kobayashi · Mika Mizunuma ·
Hiroaki Norimoto · Norio Matsuki · Yuji Ikegaya

Abstract Spontaneous neuronal activity is present in virtually all brain regions, but neither its function nor spatiotemporal patterns are fully understood. Ex vivo organotypic slice cultures may offer an opportunity to investigate some aspects of spontaneous activity, because they self-restore their networks that collapsed during slicing procedures. In hippocampal networks, we compared the levels and patterns of in vivo spontaneous activity to those in acute and cultured slices. We found that the firing rates and excitatory synaptic activity in the in vivo hippocampus are more similar to those in slice cultures compared to acute slices. The soft confidence-weighted algorithm, a machine learning technique without human bias, also revealed that hippocampal slice cultures resemble the in vivo hippocampus in terms of the overall tendency of the parameters of spontaneous activity.

Keywords Spontaneous activity · Slice culture · Machine learning algorism · Soft confidence-weighted learning

K. Okamoto and T. Ishikawa contributed equally to the present work.

K. Okamoto · T. Ishikawa · R. Abe · D. Ishikawa ·
C. Kobayashi · M. Mizunuma · H. Norimoto · N. Matsuki ·
Y. Ikegaya (✉)
Laboratory of Chemical Pharmacology, Graduate School of
Pharmaceutical Sciences, University of Tokyo, 7-3-1 Hongo,
Bunkyo-ku, Tokyo 113-0033, Japan
e-mail: ikegaya@mol.f.u-tokyo.ac.jp

Y. Ikegaya
Center for Information and Neural Networks, Suita City,
Osaka 565-0871, Japan

Introduction

The neuronal network maintains ongoing activity spontaneously even in the absence of explicit tasks, such as sensory inputs and motor outputs. Spontaneous activity prevails in many brain regions and constitutes the vast majority of the total neuronal activity, and its level is little modulated by sensory inputs [6, 29]. Spontaneous activity is reported to contribute to network development [27, 47] and neural information processing [1, 15, 18, 25, 28, 36]. Thus, elucidating spontaneous activity is critical for our understanding of the brain function; however, how spontaneous activity is stably maintained or interacts with neural information are still ill defined. This is largely because it is technically difficult to manipulate spontaneous activity in the in vivo brain.

Isolated neuronal networks, such as acute brain slice preparations, also exhibit spontaneous activity [14, 21, 22, 33]. Therefore, the in vitro preparations may provide a good experimental tool to investigate the function of spontaneous activity. However, in acute slice preparations, neurites are severely cut during slicing; approximately 90 % of the axons of pyramidal neurons are pruned in 300-μm-thick neocortical slices, whereas approximately 40 % of inhibitory basket cell axons are removed [38]. Thus, in acute slices, a significant portion of the original neuronal network is destroyed, and relative intact GABAergic axons lead to dominant inhibition against glutamatergic excitation. As a result, the level of spontaneous activity is reduced in acute slices.

Organotypic slice cultures are a technique that preserves neuronal networks ex vivo [7, 39, 46]. During a course of cultivation, pruned neurites regrow and make new synaptic connections, and the network remodels itself through self-restoration. Indeed, the synaptic connectivity and the

network complexity are likely to recover to an in vivo level [42]. This natural remodeling increases the level of spontaneous activity. Thus, slice cultures have been widely used to investigate spontaneous activity [2, 34, 43]. However, no direct comparison of spontaneous activity has been conducted between ex vivo cultured networks and in vivo intact networks, and it remains unclear to what extent the frequency and patterns of spontaneous activity in ex vivo networks replicate those in in vivo networks. In the present work, we focused on hippocampal networks and evaluated the similarity of spontaneous activity among acute slices, cultured slices, and in vivo networks.

Materials and methods

Animals

Experiments were performed with the approval of the animal experiment ethics committee at the University of Tokyo (approval no. P24-6, P24-8, and P26-5) and according to the University of Tokyo guidelines for the care and use of laboratory animals. C57BL/6J mice and Wistar/ST rats (either male or female) were housed in cages under standard laboratory conditions (12 h light/dark cycle, ad libitum access to food and water). All efforts were made to minimize the animals' suffering and the number of animals used.

In vivo electrophysiology

In vivo recordings were performed using awake, head-restrained mice. Mice (postnatal day 21–27) were anesthetized with ketamine (50 mg/kg, i.p.) and xylazine (10 mg/kg, i.p.), as described elsewhere [16]. Anesthesia was confirmed by the lack of paw withdrawal, whisker movement, and eye blink reflexes. The head skin was then removed, and the animal was implanted with a metal headholding plate. After 2 days of recovery, the head-fixation training on a custom-made stereotaxic fixture was repeated for 1–3 h per day until the implanted animal learned to remain quiet. During and after each session, the animal was rewarded with ad libitum access to sucrose-containing water. During the last three sessions, sham experiments were conducted to habituate the animal to experimental conditions and noise. After full habituation, the animal was anesthetized with a ketamine/xylazine mixture. A craniotomy (1×1 mm^2), centered 2.2 mm posterior and 2.0 mm lateral to the bregma, was performed, and the dura was surgically removed. The exposed cortical surface was covered with 1.7 % agar. Throughout the experiments, a heating pad maintained the rectal temperature at 37 °C, and the surgical region was analgesized with 0.2 % lidocaine. After recovery

from anesthesia, patch-clamp recordings were obtained using borosilicate glass electrodes (4–7 MΩ). Neurons in the CA1 pyramidal cell layer of the hippocampus were targeted for patch clamping. For voltage-clamped recordings, the intra-pipette solution consisted of the following (in mM): 140 Cs-methanesulfonate, 5 HEPES, 10 TEA-Cl, 1 EGTA, 10 2Na-phosphocreatine, and 1 Mg-ATP, pH 7.2, containing 0.2 % biocytin. sEPSCs and sIPSCs were obtained by maintaining the membrane potential at −70 and 0 mV, respectively. For cell-attached recordings, the patch pipettes were filled with artificial cerebrospinal fluid (aCSF) containing (in mM) 127 NaCl, 3.5 KCl, 1.24 KH$_2$PO$_4$, 1.2 MgSO$_4$, 2.0 CaCl$_2$, 26 NaHCO$_3$, and 10 glucose. The signals were amplified and digitized at a sampling rate of 20 kHz using a MultiClamp 700B amplifier and a Digidata 1440A digitizer that were controlled by pCLAMP 10.4 software (Molecular Devices). Experiments in which series resistance changed by >15 % during the entire recording session were discarded. Hippocampal pyramidal cells were electrophysiologically identified by their characteristic pattern of regular spiking and high-frequency bursts (HFBs; 100–300 Hz, 3–6 spikes) [17, 30].

Acute slice preparations

Acute slices were prepared from the medial to ventral part of the hippocampal formation as described elsewhere [22]. Mice (postnatal week 4–5) were anesthetized with ether and decapitated, and the brain was horizontally sliced (400 μm thick) at an angle of 12.7° to the fronto-occipital axis using a vibratome and an ice-cold oxygenated cutting solution consisting of (in mM) 222.1 sucrose, 27 NaHCO$_3$, 1.4 NaH$_2$PO$_4$, 2.5 KCl, 1 CaCl$_2$, 7 MgSO$_4$, and 0.5 ascorbic acid. Slices were allowed to recover for at least 1.5 h submerged in a chamber filled with oxygenated aCSF at room temperature.

Slice culture preparations

Entorhinal-hippocampal organotypic slices were prepared from postnatal day 7 Wistar/ST rats as described previously [19]. Rat pups were anesthetized by hypothermia and decapitated. The brains were removed and placed in aerated ice-cold Gey's balanced salt solution supplemented with 25 mM glucose. Horizontal entorhinal-hippocampal slices were cut at a thickness of 300 μm using a vibratome. The slices were placed on Omnipore membrane filters and incubated in 5 % CO$_2$ at 37 °C. The culture medium, which was composed of 50 % minimal essential medium, 25 % Hanks' balanced salt solution supplemented with 133 mM glucose, 25 % horse serum, and antibiotics, was changed every 3.5 days. Experiments were performed at 6−12 days in vitro unless otherwise specified.

In vitro electrophysiology

Recordings were performed in a submerged chamber perfused at 8 ml/min with oxygenated aCSF at 35–37 °C. Whole-cell patch-clamp recordings were obtained from hippocampal pyramidal cells visually identified under infrared differential interference contrast microscopy. Patch pipettes (3–6 MΩ) were filled with a potassium-based solution consisting of (in mM) 120 potassium gluconate, 10 KCl, 10 HEPES, 10 creatine phosphate, 4 Mg-ATP, 0.3 Na$_2$-GTP, and 0.2 EGTA or a cesium-based solution consisting of (in mM) 130 CsMeSO$_4$, 10 CsCl, 10 HEPES, 10 creatine phosphate, 4 Mg-ATP, and 0.3 Na$_2$-GTP. Spontaneous excitatory and inhibitory postsynaptic currents (EPSCs and IPSCs) were recorded at clamped voltages of −70 and 0 mV, respectively. Series resistance was not compensated.

Optical recording

For acute slices, functional multineuron calcium imaging was conducted locally loading with Oregon Green BAPTA-1AM, which can detect single spikes. Oregon Green 488 BAPTA-1AM was dissolved in DMSO containing 10 % Pluronic F-127 to yield a concentration of 200 μM. Immediately before use, this solution was diluted ten fold with aCSF and was loaded into pipettes (3–5 MΩ). The tip of the pipette was inserted into an acute hippocampal slice, and a pressure of 50–60 hPa was applied for 3–5 min using a 10-ml syringe pressurizer [22]. For cultured slices, the preparations were washed three times with oxygenated aCSF. They were transferred into a dish (35-mm diameter) containing 2 ml of the dye solution and were incubated for 1 h in a humidified incubator at 35 °C under 5 % CO$_2$ [13, 41]. After being washed, the cultured slices were incubated at 35 °C for 30 min and were mounted in a recording chamber perfused with aCSF at 35 °C. Fluorophores were excited at 488 nm with a laser diode and visualized using 507-nm-long pass emission filters. Videos were recorded at 50 frames/s acute slices using a 16× objective (0.8 numerical aperture, Nikon), a spinning-disk confocal microscope (CSU-X1; Yokogawa Electric, Tokyo, Japan), a cooled CCD camera (iXonEM+DV897; Andor Technology, Belfast, UK), and an upright microscope (Eclipse FN1; Nikon, Tokyo, Japan). The fluorescence change was measured as $(F_t−F_0)/F_0$, where F_t is the fluorescence intensity at time t and F_0 is the fluorescence intensity averaged from −10 to 10 s relative to t. Using principal component analysis and a support vector machine optimized to calcium imaging, spike-elicited calcium transients were semiautomatically detected with a custom-written program in Visual Basic [35].

Electrophysiological data analysis

Data were analyzed offline using custom MATLAB R2012b (The MathWorks) routines. In vivo spike activities were detected from cell-attached recording traces. After local filtering and smoothing, the monotonic-increasing fluctuations were detected, and events with amplitudes of 2–6 × SDs of the baseline noise were defined as spikes. False-positive events were removed by human operation. We counted any burst spiking at intervals of less than 300 ms as a single spike event in order to compare it with the rates of slow calcium transients. Synaptic events were detected from EPSC and IPSC traces. Events with amplitudes of 3–7 × SDs of the baseline noise after local filtering and smoothing were defined as synaptic events. To remove the possible artificial effect of high-access resistance recordings in vivo, the sEPSG amplitude was software-based corrected as described previously [44]. Then we obtained excitatory and inhibitory postsynaptic conductances (EPSGs and IPSGs) from instantaneous current amplitudes (i.e., EPSG and IPSG amplitudes, respectively) using the following potential-to-current relationship:

$$I_m = C_m\left(\frac{dV_m}{dt}\right) + g_{exc}(V_m - E_{exc}) + g_{inh}(V_m - E_{inh}) + g_{leak}(V_m - E_{leak}),$$

in which I_m represents the membrane current, C_m the membrane capacitance, V_m the membrane potential, $g_{exc}/g_{inh}/g_{leak}$ the excitatory/inhibitory/leak conductances, and $E_{exc}/E_{inh}/E_{leak}$ the excitatory/inhibitory/leak potential driving forces. dV_m and g_{leak} were thought to be approximated to 0. E_{inh} and E_{exc} were assumed to be −70 or 0 mV, respectively, which were clamped voltages to isolate EPSCs and IPSCs, respectively. These assumptions allowed us to calculate EPSGs and IPSGs from EPSCs and IPSCs. CV, skewness, and kurtosis were calculated from the EPSG and IPSG events.

Multidimentional scaling

We used 11 EPSGs and 14 IPSGs in vivo, 35 EPSGs and 14 IPSGs in acute slices, and 15 EPSGs and 24 IPSGs in slice cultures. The parameters (vector) of postsynaptic conductances (PSGs) consisted of the mean, coefficient of variation (CV), skewness, and kurtosis of PSG amplitude and the PSG event frequency. We calculated the Euclidean distance between each pair of vector's Z score and applied the conventional nonmetric multidimensional scaling (MDS), a dimension reduction technique for illustration purpose, to these pairwise distances. The MDS plot indicates relative pairwise distances between vectors. For the MDS results, a dendrogram was constructed using Ward's method, a hierarchical clustering algorithm. MDS and

dendrogram were calculated using MATLAB R2012b (The Mathworks) routines.

Soft confidence-weighted learning (SCW)

The SCW learning, a machine learning algorithm, consisted of two steps, i.e., the learning phase and test phase. In the learning phase, the algorithm was tuned to create the most appropriate criteria, which were later used to classify another set of preparations. More specifically, the SCW machine is exposed to the data sets of two preparations, slice cultures and acute slices (Fig. 4a, b), and in vivo preparations and acute slices (Fig. 4c, d). Each data set consisted of four parameters, i.e., the CV, skewness, and kurtosis of PSGs and the PSG event frequency. In the test phase, the trained SCW predicted (classified) a newly given data set as slice cultures or acute slices (Fig. 4a, b) and in vivo preparations or acute slices (Fig. 4c, d) based on the criteria obtained in the learning phase. All routines were written in MATLAB (The Math Works). The SCW learning code was downloaded from: http://www.cais.ntu.edu.sg/~chhoi/libol/about.html. We used the SCW-II algorithm.

Learning phase: We used 11 EPSGs and 14 IPSGs in vivo, 35 EPSGs and 14 IPSGs in acute slices, and 15 EPSGs and 24 IPSGs in slice cultures. In the classification of in vivo preparations, the SCW was exposed sequentially to individual data sets of acute and cultured slices. We used each data set that reflected the characteristic PSG parameters as a supervise vector, and each supervise vector was labeled as −1 (acute slices) or +1 (culture slice). During the learning, SCW gradually updated the weighted vector W, which was finally expected to be used for the most appropriate classification. Likewise, for classification of slice culture preparations, SCW was sequentially exposed to the data sets of acute slices and in vivo preparations, which are labeled as −1 or +1, respectively.

Test phase: SCW was newly given other data sets and was forced to judge the similarity of the preparations, based on the weighted vector W. We defined the SCW score as the relative distance from the criterion of classification as follows:

$$SCW\ score = W^T x_t,$$

in which x_t is the data set of the preparation. The SCW score takes a positive value if the vector x_t is similar to cultured slices (Fig. 4a, b) or in vivo preparations (Fig. 4c, d).

Statistics

We reported the data as the mean ± SD. Median test or Kruskal-Wallis test, Mann-Whitney's U test, and Bonferroni correction were performed to assess the significance of the differences. P values <0.05 were considered statistically significant.

Results

Firing rates are similar between in vivo networks and cultured slices

Spiking activity is the major output from a neuron. If spontaneous activity in in vivo and in vitro preparations shares common information infrastructures, the spike patterns are expected to be similar. We calculated the mean firing rates of hippocampal CA1 and CA3 pyramidal cells in in vivo preparations, cultured slices, and acute slices. Spontaneous action potentials in vivo were recorded from awake mice using the cell-attached patch-clamp technique (Fig. 1a). For each cell, the activity was monitored for 2–5 min. In in vitro preparations, we recorded action potentials using functional multineuron calcium imaging in order to increase the throughput of data collection. Action potentials of a neuron evoke transient calcium increases in the cell body. The kinetics of individual calcium events are so slow that action potentials at intervals of less than 300 ms cannot be resolved in calcium traces and are captured in a single event [35]. To directly compare the in vivo and in vitro spike rates, we regarded any burst at interspike intervals of less than 300 ms as a single calcium spike. Then, we re-counted the number of total "spikes" for the entire recording period.

In acute slices and cultured slices, we recorded spontaneous firings using functional multineuron calcium imaging (Fig. 1b, c). The length of a video ranged from 2 to 10 min. For each cell, we counted the total number of individual calcium transients and calculated the "spike" rates. The mean firing rates of acute slices were $9.3 \times 10^{-6} \pm 5.5 \times 10^{-6}$ Hz (Fig. 1d; mean ± SD of 1,056 cells from 15 slices) and were significantly lower than that of cultured slices (0.048 ± 0.042 Hz of 1,178 cells from 12 slices; $P = 6.0 \times 10^{-6}$, Median test) and in vivo preparations (0.14 ± 0.21 Hz of 175 cells from 116 mice; $P = 1.0 \times 10^{-5}$). The firing rates of cultured slices were lower than those of in vivo preparations, but the difference was not statistically significant ($P = 0.38$). Note that the mean firing rates include silent cells that did not show spiking activity during our observation period. The ratios of silent cells in in vivo preparations (39 %; 68 of 175 cells) and cultured slices (38 %; 450 of 1178 cells) in cultured slices were significantly higher than those in acute slices (62 %; 658 of 1058 cells; $P = 1.2 \times 10^{-8}$ versus in vivo, $P = 2.2 \times 10^{-16}$ versus cultured slices, Fisher's exact test). These results indicate that, for the mean firing
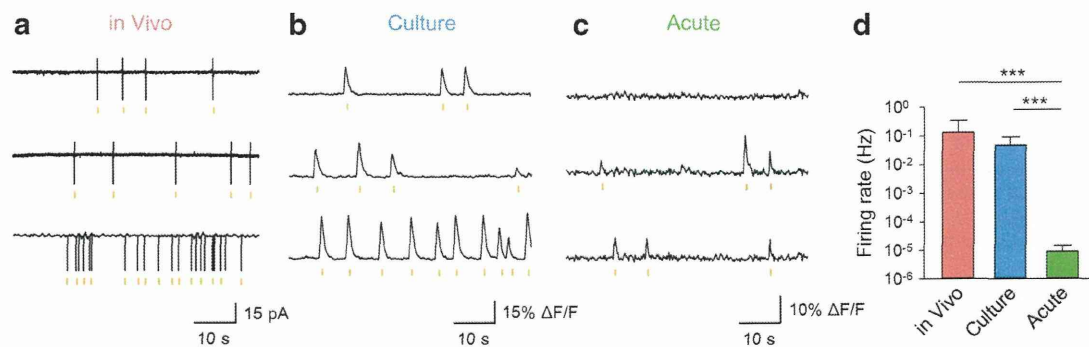
Fig. 1 Comparison of the spontaneous firing rates of CA1 neurons between the in vivo, cultured, and acute hippocampal network. Representative traces of in vivo cell-attached recording (**a**) and calcium imaging from the CA1 and CA3 pyramidal cell layer in a slice culture (**b**) and an acute slice (**c**). *Orange dots below the traces* indicate the timings of spikes. **d** The mean ± SD firing rates of 175 CA1 neurons of in vivo preparations (*red*), 1,178 neurons from 12 slice cultures (*blue*), and 1,056 neurons from 15 acute slices (*green*). ***$P < 0.001$, median test

rates, culture slices are more similar to in vivo conditions compared to acute slices.

sEPSGs are similar between in vivo networks and cultured slices

We next focused on the similarity of spontaneous synaptic activity. Using voltage-clamp recordings at −70 mV, we recorded sEPSGs from hippocampal pyramidal neurons in in vivo preparations, cultured slices, and acute slices for 1–3 min (Fig. 2a, b, c). Unlike the all-or-none fashion of spiking outputs, the intensity of synaptic inputs fluctuates continuously. For each neuron, therefore, we calculated the mean amplitude, CV, skewness, and kurtosis of its sEPSG trace (Fig. 2d). Then, data were collected from 11 cells in 11 mice (in vivo), 15 cells in 8 slice cultures, and 35 cells in 14 acute slices. The EPSG amplitude in cultured slices was 1.13 ± 0.94 nS (mean ± SD) and was significantly higher than that of in vivo preparations $(0.24 \pm 0.07$ nS; $P = 6.0 \times 10^{-3}$, $U = 25$, Mann-Whitney's U test with Bonferroni correction after Kruskal-Wallis test) and of acute slices $(0.24 \pm 0.06$ nS; $P = 2.70$, $U = 198$). The CV of cultured slices was 1.09 ± 0.59 and was not significantly different from that of in vivo preparations $(0.82 \pm 0.39$; $P = 0.23$, $U = 48$). The CV of acute slices was 0.50 ± 0.23 and was significantly higher than those of in vivo preparations $(P = 9.7 \times 10^{-3}, U = 81)$ and of slice cultures $(P = 3.4 \times 10^{-7}, U = 38)$. Neither the skewness (in vivo: 3.95 ± 4.64, slice culture: 4.23 ± 5.29, acute slice: 2.18 ± 1.03) nor kurtosis (in vivo: 50.3 ± 103.6, slice culture: 62.1 ± 120.9, acute slice: 10.4 ± 9.0) differed among three preparations (skewness: $P = 0.73$, $\chi^2 = 0.63$; kurtosis: $P = 0.31$, $\chi^2 = 2.36$; Kruskal-Wallis test). We also detected individual EPSG events and calculated the mean event frequency (Fig. 2e). The event frequencies of in vivo preparations $(10.9 \pm 9.3$ Hz) and
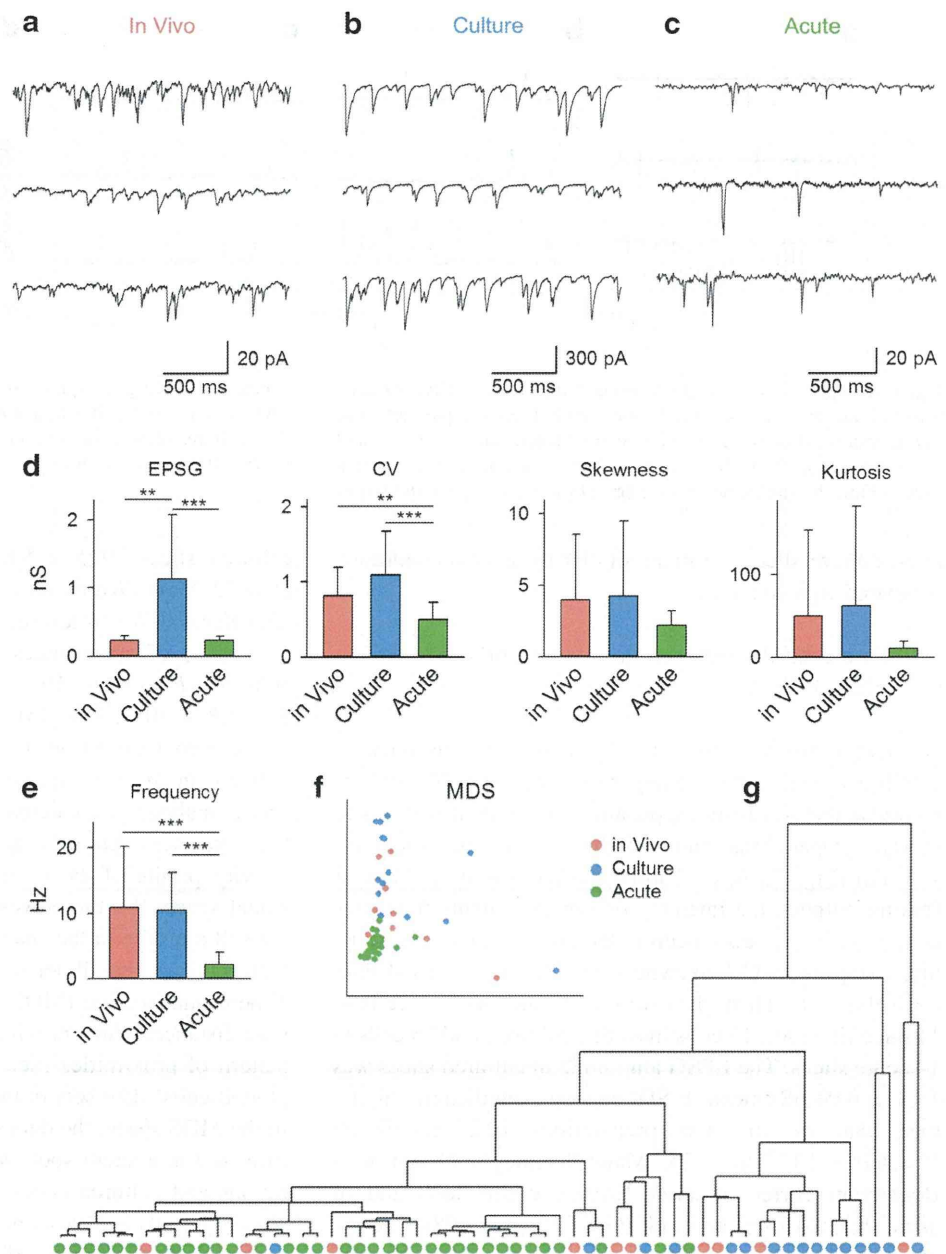
cultured slices $(10.5 \pm 5.8$ Hz) did not differ $(P = 1.0$, $U = 72$; Mann-Whitney's U test with Bonferroni correction after Kruskal-Wallis test) and were both significantly higher than those of acute slices $(2.18 \pm 1.93$ Hz; versus slice culture: $P = 5.4 \times 10^{-4}$, $U = 55$; versus in vivo: $P = 1.8 \times 10^{-9}, U = 15)$.

We next focused on the parameters of individual cells rather than the measurements of pooled data sets. In the above analyses, we calculated five parameters, i.e., mean, CV, skewness, kurtosis, and event frequency. Thus, the activity profile of each cell was depicted in five-dimensional space. We thus investigated the relative location of the cell's profile in the space. For illustration purposes, we first reduced the dimension of the profile using multidimensional scaling (MDS), based on the Z-score of pairwise distance, which provides a visual representation of the pattern of proximities (i.e., similarities) among cells' and plotted cells' data sets in two-dimensional space (Fig. 2f). In the MDS space, the data sets of acute slices tended to be localized in a small spot, whereas those of in vivo preparations and cultured slices tended to be more widely dispersed with their data set areas overlapping each other. We analyzed these data set distributions using dendrogram-based clustering (Fig. 2g). The cells of in vivo preparations and slice cultures were ranked in an intermingled order, but the cells in acute slices tended to be more separated from the two other groups. Therefore, as a whole, sEPSCs of in vivo preparations were similar to those of slice cultures compared to those of acute slices.

sIPSGs are not similar between in vivo networks and cultured slices

We performed the same analyses for sIPSGs. sIPSGs were recorded from 14 cells in 14 mice (in vivo), 24 cells in 9 slice cultures, and 14 cells in 8 acute slices (Fig. 3a, b, c).

Fig. 2 Comparison of sEPSGs among in vivo, cultured, and acute hippocampal networks. Representative sEPSG traces recorded from three CA1 pyramidal neurons each in in vivo preparations (**a**), in a slice culture (**b**), and in an acute slice (**c**). **d** The mean, CV, skewness, and kurtosis of the sEPSG fluctuations are calculated for 11 cells of in vivo preparations (*red*), 15 cells of slice cultures (*blue*), and 35 cells of acute slices (*green*). **P < 0.01, ***P < 0.001, Mann-Whitney's U test with Bonferroni correction. *Error bars* are SDs. **e** The frequency of sEPSG events. Data are mean ± SD of 11 cells (in vivo), 15 cells (culture), and 35 cells (acute). ***P < 0.001, Mann-Whitney's U test with Bonferroni correction. **f** The five parameters of individual neurons were dimension reduced to the 2D space using multidimensional scaling (MDS). Each *dot* indicates a single cell, and its color corresponds to the cohort, in vivo (*red*), slice culture (*blue*), and acute slice (*green*). The data similarity is expressed as the pairwise Euclidean distance. **g** The MDS results in **f** are classified as a dendrogram

The mean IPSG amplitude in cultured slices was 1.83 ± 0.84 nS (mean ± SD) and was significantly higher than that of in vivo preparations (Fig. 3d; 0.57 ± 0.17 nS; $P = 6.0 \times 10^{-8}$, $U = 9$, Mann-Whitney's U test with Bonferroni correction after Kruskal-Wallis test) and that of acute slices (1.19 ± 0.41 nS; $P = 0.017$, $U = 78$). The amplitude in acute slices was also significantly higher than that of in vivo preparations ($P = 2.8 \times 10^{-6}$, $U = 191$). The CV of sIPSGs in cultured slices was 1.02 ± 0.21 and was significantly higher than that of in vivo preparations (0.79 ± 0.25; $P = 0.013$, $U = 76$) and of acute slices

$(0.77 \pm 0.18$; $P = 3.1 \times 10^{-3}$, $U = 63$). Neither the skewness (in vivo: 2.75 ± 1.68, slice culture: 2.28 ± 0.99, acute slice: 2.58 ± 2.07) nor kurtosis (in vivo: 17.0 ± 19.0, slice culture: 11.2 ± 8.9, acute slice: 15.2 ± 22.2) differed among three preparations (skewness: $P = 0.70$, $\chi^2 = 0.71$, kurtosis: $P = 0.27$, $\chi^2 = 2.59$; Kruskal–Wallis test). The sIPSG event frequencies of in vivo preparations (11.9 ± 8.7 Hz) and cultured slices (5.59 ± 2.88 Hz) did not differ (Fig. 3e; $P = 0.12$, $U = 236$; Mann-Whitney's U test and Bonferroni correction after Kruskal-Wallis test) and were both significantly higher than those of acute slices

Fig. 3 Comparison of sIPSGs among in vivo, cultured, and acute hippocampal networks. Representative sIPSG traces recorded from three CA1 pyramidal neurons each in in vivo preparations (**a**), in a slice culture (**b**), and in an acute slice (**c**). **d** The mean, CV, skewness, and kurtosis of the sIPSG fluctuations are calculated for 14 cells of in vivo preparations (*red*), 24 cells of slice cultures (*blue*), and 14 cells of acute slices (*green*). *$P < 0.05$, **$P < 0.01$, ***$P < 0.001$, Mann-Whitney's U test with Bonferroni correction. *Error bars* are SDs. **e** The mean ± SD of sIPSG event frequency. ***$P < 0.001$, Mann-Whitney's U test with Bonferroni correction. **f** The five parameters of individual neurons were dimension reduced to the 2D space using multidimensional scaling (MDS). Each *dot* indicates a single cell, and its color corresponds to the cohort, in vivo (*red*), slice culture (*blue*), and acute slice (*green*). The data similarity is expressed as the pairwise Euclidean distance. **g** The MDS results in **f** are classified in a dendrogram
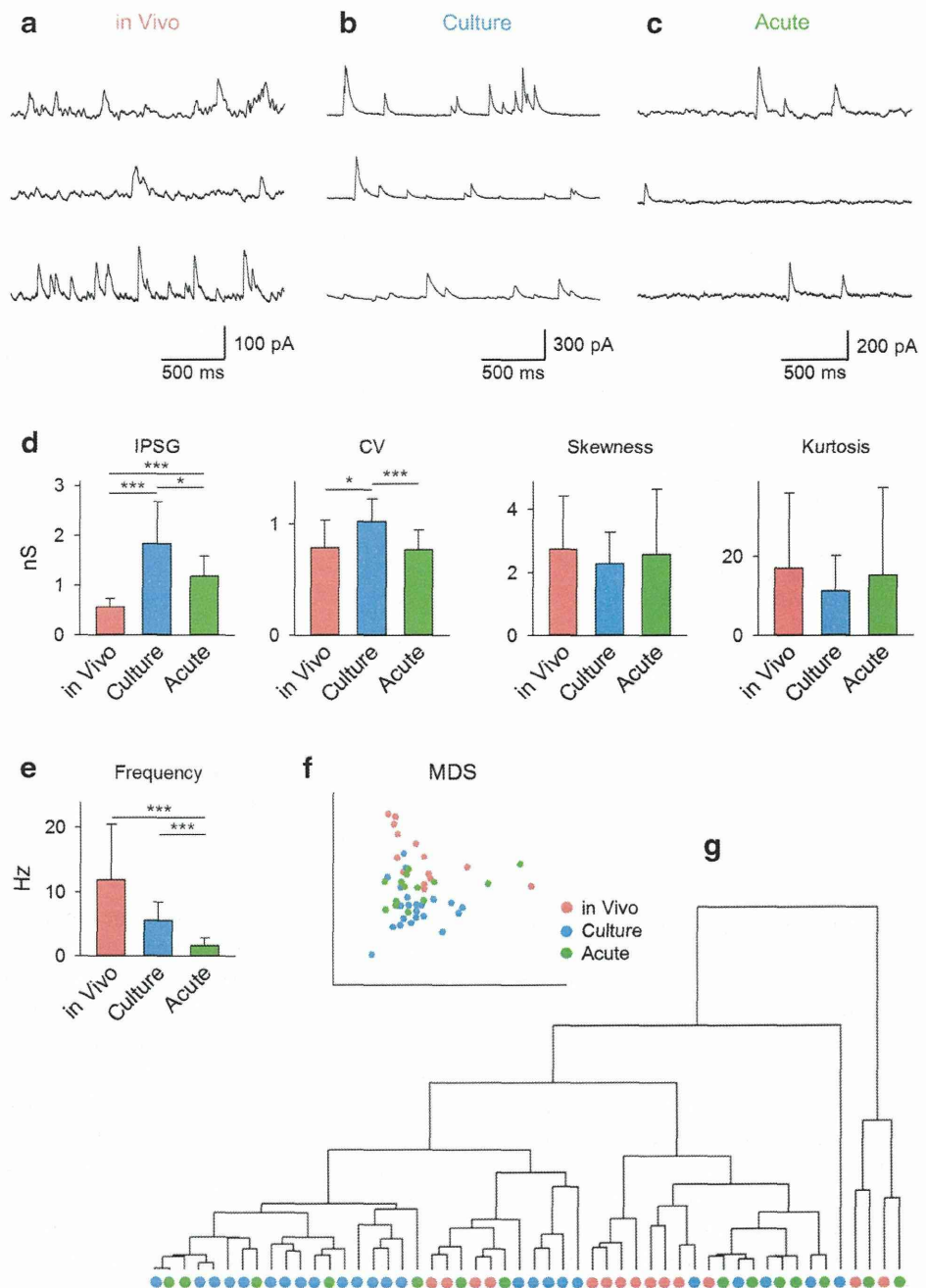
(1.64 ± 1.23 Hz; versus slice culture: $P = 1.1 \times 10^{-4}$, $U = 31$; versus in vivo: $P = 3.0 \times 10^{-4}$, $U = 19$).

Using MDS, we plotted the sIPSG data sets of individual cells in the two-dimensional space (Fig. 3f). The data sets of three groups exhibited no clear spatial separations in the MDS space. These overlapped distributions were also confirmed in the dendrogram of the MDS data (Fig. 3g). Therefore, these simple comparisons failed to indicate which is similar to in vivo preparations, slice cultures, or acute slices.

SCW classifies data sets of cultured slices as in vivo-like

The MDS algorithm has been used as an integral classification method, but it may not completely capture the net difference in the multidimensional features of synaptic activity, because MDS is designed to treat all the parameters equivalently. Therefore, we adopted the SCW learning, a recently invented supervised machine learning algorithm [45], to consider the latent difference underlying